

This work was written as part of one of the author's official duties as an Employee of the United States Government and is therefore a work of the United States Government. In accordance with 17 U.S.C. 105, no copyright protection is available for such works under U.S. Law.

Public Domain Mark 1.0

<https://creativecommons.org/publicdomain/mark/1.0/>

Access to this work was provided by the University of Maryland, Baltimore County (UMBC) ScholarWorks@UMBC digital repository on the Maryland Shared Open Access (MD-SOAR) platform.

Please provide feedback

Please support the ScholarWorks@UMBC repository by emailing scholarworks-group@umbc.edu and telling us what having access to this work means to you and why it's important to you. Thank you.

THREE-FLUID, THREE-DIMENSIONAL MAGNETOHYDRODYNAMIC SOLAR WIND MODEL WITH EDDY VISCOSITY AND TURBULENT RESISTIVITY

ARCADI V. USMANOV^{1,3}, MELVYN L. GOLDSTEIN², AND WILLIAM H. MATTHAEUS¹

¹ Department of Physics and Astronomy, University of Delaware, Newark, DE 19716, USA; arcadi.usmanov@nasa.gov

² Code 672, NASA Goddard Space Flight Center, Greenbelt, MD 20771, USA

Received 2013 November 11; accepted 2014 April 29; published 2014 May 20

ABSTRACT

We have developed a three-fluid, three-dimensional magnetohydrodynamic solar wind model that incorporates turbulence transport, eddy viscosity, turbulent resistivity, and turbulent heating. The solar wind plasma is described as a system of co-moving solar wind protons, electrons, and interstellar pickup protons, with separate energy equations for each species. Numerical steady-state solutions of Reynolds-averaged solar wind equations coupled with turbulence transport equations for turbulence energy, cross helicity, and correlation length are obtained by the time relaxation method in the corotating with the Sun frame of reference in the region from 0.3 to 100 AU (but still inside the termination shock). The model equations include the effects of electron heat conduction, Coulomb collisions, photoionization of interstellar hydrogen atoms and their charge exchange with the solar wind protons, turbulence energy generation by pickup protons, and turbulent heating of solar wind protons and electrons. The turbulence transport model is based on the Reynolds decomposition and turbulence phenomenologies that describe the conversion of fluctuation energy into heat due to a turbulent cascade. In addition to using separate energy equations for the solar wind protons and electrons, a significant improvement over our previous work is that the turbulence model now uses an eddy viscosity approximation for the Reynolds stress tensor and the mean turbulent electric field. The approximation allows the turbulence model to account for driving of turbulence by large-scale velocity gradients. Using either a dipole approximation for the solar magnetic field or synoptic solar magnetograms from the Wilcox Solar Observatory for assigning boundary conditions at the coronal base, we apply the model to study the global structure of the solar wind and its three-dimensional properties, including embedded turbulence, heating, and acceleration throughout the heliosphere. The model results are compared with plasma and magnetic field observations on *WIND*, *Ulysses*, and *Voyager 2* spacecraft.

Key words: magnetic fields – magnetohydrodynamics (MHD) – methods: numerical – solar wind – turbulence

Online-only material: color figures

1. INTRODUCTION

The solar wind plasma is composed primarily of protons and electrons and is virtually collisionless beyond the inner corona. Sturrock & Hartle (1966) and Hartle & Sturrock (1968) were the first to note that the collisional energy exchange between the two species is too weak to treat the solar wind as a one-fluid plasma with a single temperature. Treating the protons and electrons with separate energy equations, they developed the first two-fluid solar wind model with energy exchange between the two species by Coulomb collisions. The model assumed that the bulk velocity was the same for both species and the electron mass was neglected in comparison with the proton mass. It appears more appropriate to refer to Sturrock and Hartle’s approach as “two-temperature,” but the term “two-fluid” gained universal acceptance in the scientific community for solar wind models of this type. There exist a multitude of two-fluid models in one dimension (e.g., Hartle & Barnes 1970; Leer & Axford 1972; Hollweg 1973; Durney 1973; Esser et al. 1986; Cuperman et al. 1988; Sandbæk et al. 1992; Sandbæk & Leer 1994; Habbal et al. 1995; Tu & Marsch 1997) and two dimensions (e.g., Suess et al. 1999; Davila & Ofman 1999; Chen & Hu 2001; Hu et al. 2003a, 2003b; Endeve et al. 2004; Li et al. 2004). To the best of our knowledge, the only fully three-dimensional two-fluid solar

wind models are the recent ones of van der Holst et al. (2010) and Sokolov et al. (2013).

A small fraction of solar wind protons undergo collisional charge exchange with interstellar hydrogen that enters the heliosphere due to the Sun’s motion through the partially ionized local interstellar medium. The charge exchange process gives rise to a population of protons that are picked up by the heliospheric magnetic field and entrained into the solar wind. This population of pickup protons is further enhanced by photoionization and electron impact ionization of the interstellar hydrogen. Even though the density of pickup protons is much smaller than that of solar wind protons, the pickup protons profoundly affect the solar wind in the outer heliosphere. For example, the momentum loss due to entrainment of the newborn pickup protons causes a significant deceleration of the wind (e.g., Semar 1970; Holzer 1972) and an overall compression of the magnetic field in the outer heliosphere (Zank 1999; Usmanov et al. 2012). Furthermore, the thermal pressure of the pickup protons dominates the internal energy of the wind (Burlaga et al. 1994, 1996) and weakens corotating interaction regions (Usmanov et al. 2012).

A number of one-fluid solar wind models that account for pickup protons assume that due to wave-particle interactions the pickup protons are assimilated with the solar wind protons much faster than it takes for the solar wind flow to convect the pickup protons out of the heliosphere (e.g., Zank & Pauls 1997; Wang et al. 2000; Pogorelov et al. 2009). The assumption of quick assimilation results in a substantial amount of energy absorbed

³ Also at Code 673, NASA Goddard Space Flight Center, Greenbelt, MD 20771, USA.

by solar wind protons and a quick increase of predicted proton temperature with heliocentric distance in the outer heliosphere. The increase is steep and obviously inconsistent with *Voyager 2* observations. Noting that the energy exchange between solar wind protons and pickup protons is in fact too weak for their quick assimilation, Isenberg (1986) constructed a three-fluid one-dimensional (radial) solar wind model with co-moving solar wind protons, electrons, and pickup protons, and separate energy equations for each species. The model assumes that there is no energy exchange between the two proton species and that the solar wind protons cool with distance almost adiabatically. Isenberg's approach was further developed in the one-dimensional models of Whang et al. (1995, 2003), Whang (1998), and three-dimensional models of Usmanov & Goldstein (2006) and Detman et al. (2011).

Wang & Richardson (2001) suggested that only a certain fraction of the initial energy of pickup protons is transferred to the solar wind protons as a result of wave-particle interactions. By introducing into the Isenberg (1986) model a parameter that represents the ratio of the energy absorbed by solar wind protons to the energy provided by the pickup process, they demonstrated that a small percentage ($\sim 5\%$) of the pickup proton energy is sufficient to reproduce the temperature profile observed by *Voyager 2*. A similar idea is used in the turbulence transport models (Williams et al. 1995; Matthaeus et al. 1999, 2004; Smith et al. 2001, 2006; Isenberg et al. 2003, 2010; Breech et al. 2008, 2009) that describe the heating of solar wind protons by pickup protons through the generation of turbulence and its subsequent dissipation via a turbulent cascade. In those models, the background solar wind and magnetic field parameters are pre-defined and the contribution of pickup protons is modeled by a source term in the equation for turbulent energy with a coefficient introduced to represent the fraction of pickup proton energy converted into turbulent fluctuations. Related methods, based on a kinetic description of pickup protons and spectral wave energy density, have been developed by Isenberg (2005), Chalov et al. (2006), and Gamayunov et al. (2012).

Applying the Reynolds averaging approach, Usmanov et al. (2009, 2011) have incorporated the turbulence transport model of Breech et al. (2008) into their global solar wind simulation and developed an axisymmetric solar wind model with turbulence transport for the region from 0.3 to 100 AU by solving simultaneously the solar wind equations along with turbulence transport equations. Continuing with this approach and merging it with the one of Usmanov & Goldstein (2006), Usmanov et al. (2012) developed a two-fluid fully three-dimensional solar wind model that treats interstellar pickup protons as a separate fluid and incorporates transport of turbulence and turbulent heating. A similar approach was taken recently by Kryukov et al. (2012). Several important effects of pickup protons were studied quantitatively by Usmanov et al. (2012): the deceleration of the solar wind as a result of the momentum transfer from the solar wind protons to pickup protons, the heating of the solar wind plasma by dissipation of turbulent energy, the compression of the predominantly azimuthal magnetic field in the outer heliosphere as a result of the deceleration, and the weakening of the corotating interaction regions due to the deceleration and the thermal pressure of pickup protons.

A significant limitation of the modeling approach of Usmanov et al. (2012) is that it treats solar wind protons and electrons as a single fluid and assumes that the thermal pressures of solar wind protons and electrons are equal. Consequently, the solar wind proton and electron temperatures are implied to be virtually

equal and the turbulent heating is implicitly equipartitioned between the protons and electrons, as is the heating due to the electron heat conduction. An additional limitation is related to the turbulence transport model adopted by Usmanov et al. (2009, 2011, 2012): the approximation for the Reynolds stress tensor is based on the assumption of structural similarity (i.e., each element of a correlation tensor is assumed to be proportional to the trace of the tensor) and an assumed symmetry of fluctuations (the fluctuations are postulated to be transverse to the mean magnetic field \mathbf{B}). This approximation does not account for the effects of large-scale velocity gradients driving turbulence ("shear driving" or "phase mixing"; Ruderman et al. 1999).

In this paper, we present a three-fluid extension of the model of Usmanov et al. (2012) with separate energy equations for solar wind protons, electrons, and pickup protons, and with eddy viscosity and turbulent resistivity approximations for the Reynolds stress tensor and the mean turbulent electric field. The approximations are based on the results from the two-scale direct interaction approximation (TSDIA) of Yoshizawa (1998) and, in contrast to our previous work, they account for driving of turbulence by velocity shears. These technical improvements in modeling the physics of the solar wind represent important steps in achieving more realistic pathways for energy exchange between fields and particles across all important scales. Even though the outer boundary of the computation region has been arbitrarily chosen at 100 AU, it should be noted that the model presented in this paper is still a model of supersonic/super-Alfvénic solar wind that does not include the interaction of the heliosphere with the interstellar medium. We first describe in detail in Section 2 the equations that govern the mean solar wind flow and the employed turbulence model. The boundary conditions and model parameters are also discussed. The results of simulation and comparisons with spacecraft observations are presented in Section 3. We conclude with a summary of our results and a discussion of limitations and future extensions of our model in Section 4.

2. MODEL FORMULATION

2.1. The Three-fluid Governing Equations

The solar wind is assumed to be a fully ionized plasma composed of electrons and two populations of protons: solar wind protons and interstellar pickup protons. We describe the three species by fluid equations with separate mass and energy equations and assume that the bulk velocity is the same for all three species (Isenberg 1986). Following Whang et al. (1995), Usmanov & Goldstein (2006), Breech et al. (2009), Whang (2010), and Usmanov et al. (2011, 2012), the time-dependent three-fluid MHD equations in the corotating with the Sun frame of reference are written as

$$\frac{\partial \tilde{N}_S}{\partial t} + \nabla \cdot (\tilde{N}_S \tilde{\mathbf{v}}) = -q_{ex1}, \quad (1)$$

$$\frac{\partial \tilde{\mathbf{v}}}{\partial t} + (\tilde{\mathbf{v}} \cdot \nabla) \tilde{\mathbf{v}} + \frac{1}{\tilde{\rho}} \nabla (\tilde{P}_S + \tilde{P}_E + \tilde{P}_I) - \frac{(\nabla \times \tilde{\mathbf{B}}) \times \tilde{\mathbf{B}}}{4\pi \tilde{\rho}} + \frac{G M_\odot}{r^2} \hat{\mathbf{r}} + 2\boldsymbol{\Omega} \times \tilde{\mathbf{v}} + \boldsymbol{\Omega} \times (\boldsymbol{\Omega} \times \mathbf{r}) = -\frac{1}{\tilde{\rho}} (q_{ex1} + q_{ex2} + q_{ph}) m_p \tilde{\mathbf{u}}, \quad (2)$$

$$\frac{\partial \tilde{\mathbf{B}}}{\partial t} = \nabla \times (\tilde{\mathbf{v}} \times \tilde{\mathbf{B}}), \quad (3)$$

$$\frac{\partial \tilde{P}_S}{\partial t} + (\tilde{\mathbf{v}} \cdot \nabla) \tilde{P}_S + \gamma \tilde{P}_S \nabla \cdot \tilde{\mathbf{v}} + \frac{\gamma \tilde{P}_S}{\tilde{N}_S} q_{\text{ex1}} + (\gamma - 1) \frac{\tilde{P}_S - \tilde{P}_E}{\tau_{\text{SE}}} = f_p Q_1(\mathbf{r}), \quad (4)$$

$$\frac{\partial \tilde{N}_I}{\partial t} + \nabla \cdot (\tilde{N}_I \tilde{\mathbf{v}}) = q_{\text{ex1}} + q_{\text{ph}}, \quad (5)$$

$$\frac{\partial \tilde{P}_I}{\partial t} + (\tilde{\mathbf{v}} \cdot \nabla) \tilde{P}_I + \frac{5}{3} \tilde{P}_I \nabla \cdot \tilde{\mathbf{v}} = (q_{\text{ex1}} + q_{\text{ph}}) \frac{m_p \tilde{u}^2}{3} - Q_2(\mathbf{r}), \quad (6)$$

$$\frac{\partial \tilde{P}_E}{\partial t} + (\tilde{\mathbf{v}} \cdot \nabla) \tilde{P}_E + \gamma \tilde{P}_E \nabla \cdot \tilde{\mathbf{v}} - \frac{\gamma \tilde{P}_E}{\tilde{N}_E} q_{\text{ph}} + (\gamma - 1) \left(\frac{\tilde{P}_E - \tilde{P}_S}{\tau_{\text{SE}}} + \nabla \cdot \mathbf{q}_H \right) = (1 - f_p) Q_1(\mathbf{r}), \quad (7)$$

where the independent variables are time t and the heliocentric position vector \mathbf{r} . The dependent quantities are the number densities of solar wind protons \tilde{N}_S and pickup protons \tilde{N}_I , the velocity in the corotating with the Sun frame of reference $\tilde{\mathbf{v}}$, the magnetic field $\tilde{\mathbf{B}}$, and the thermal pressures of solar wind protons \tilde{P}_S , electrons \tilde{P}_E , and pickup protons \tilde{P}_I . We neglect the electron mass in comparison with the mass of proton m_p and, as a result, the mass density $\tilde{\rho} = m_p(\tilde{N}_S + \tilde{N}_I)$. The requirement of charge neutrality implies that the electron number density $\tilde{N}_E = \tilde{N}_S + \tilde{N}_I$. Other symbols are: the velocity in the inertial frame $\tilde{\mathbf{u}} = \tilde{\mathbf{v}} + \boldsymbol{\Omega} \times \mathbf{r}$, the electron heat flux \mathbf{q}_H , the production rates of pickup protons from interstellar hydrogen atoms by charge exchange with solar wind protons q_{ex1} and with interstellar pickup protons q_{ex2} , and by photoionization q_{ph} , the solar rotation rate $\boldsymbol{\Omega}$, the universal gravitation constant G , the solar mass M_\odot , the unit vector in the radial direction $\hat{\mathbf{r}}$, and the adiabatic index γ . The sources of energy deposition/extraction are the turbulent heating $Q_1(\mathbf{r})$ apportioned between solar wind protons and electrons with f_p being the fraction, and the energy lost by pickup protons to feed the turbulent fluctuations $Q_2(\mathbf{r})$. The terms with the collision time scale τ_{SE} are assumed to model the energy exchange between the solar wind protons and electrons by Coulomb collisions (see Breech et al. 2009). The heat flux carried by solar wind protons is neglected. We neglect also alpha particles, which commonly have 5% of the solar wind mass and thus 20% of the solar wind momentum (e.g., Meyer-Vernet 2007), and the electron impact ionization of interstellar hydrogen, which is relatively small at 1 AU ($\lesssim 10\%$ of the total ionization rate) and becomes negligible at larger heliocentric distances as the electron temperature decreases (e.g., Rucinski & Fahr 1989; Isenberg & Feldman 1995).

The governing system of equations (Equations (1)–(7)) differs from that in Usmanov et al. (2012) by the appearance of two new dependent variables—the solar wind proton \tilde{P}_S and electron \tilde{P}_E pressures—and, correspondingly, two equations that separately track the proton and electron internal energies instead of a single equation for the combined pressure $\tilde{P} = \tilde{P}_S + \tilde{P}_E$.

2.2. The Reynolds Averaged Solar Wind Equations

To introduce turbulence effects into the mean-flow Equations (1)–(7) we use the Reynolds decomposition of physical variables into mean and fluctuating parts $\tilde{\mathbf{a}} = \mathbf{a} + \mathbf{a}'$, where $\tilde{\mathbf{a}}$

is any dependent variable. The ensemble average $\langle \tilde{\mathbf{a}} \rangle = \mathbf{a}$, and, by construction, $\langle \mathbf{a}' \rangle = 0$. Assuming that the turbulence is locally incompressible ($N'_S = N'_I = 0$) and applying the Reynolds averaging, we obtain the following mean-flow equations

$$\frac{\partial N_S}{\partial t} + \nabla \cdot (N_S \mathbf{v}) = -q_{\text{ex1}}, \quad (8)$$

$$\begin{aligned} \frac{\partial(\rho \mathbf{v})}{\partial t} + \nabla \cdot \left[\rho \mathbf{v} \mathbf{v} - \frac{1}{4\pi} \mathbf{B} \mathbf{B} \right. \\ \left. + \left(P_S + P_E + P_I + \frac{\langle B'^2 \rangle}{8\pi} + \frac{B^2}{8\pi} \right) \mathbf{I} + \mathcal{R} \right] \\ + \rho \left[\frac{GM_\odot}{r^2} \hat{\mathbf{r}} + 2\boldsymbol{\Omega} \times \mathbf{v} + \boldsymbol{\Omega} \times (\boldsymbol{\Omega} \times \mathbf{r}) \right] \\ = -m_p [(q_{\text{ex1}} + q_{\text{ex2}}) \mathbf{u} + q_{\text{ph}} \boldsymbol{\Omega} \times \mathbf{r}], \end{aligned} \quad (9)$$

$$\frac{\partial \mathbf{B}}{\partial t} = \nabla \times (\mathbf{v} \times \mathbf{B} + \sqrt{4\pi\rho} \boldsymbol{\varepsilon}_m), \quad (10)$$

$$\begin{aligned} \frac{\partial P_S}{\partial t} + (\mathbf{v} \cdot \nabla) P_S + \gamma P_S \nabla \cdot \mathbf{v} + \frac{\gamma P_S}{N_S} q_{\text{ex1}} + (\gamma - 1) \frac{P_S - P_E}{\tau_{\text{SE}}} \\ + \langle (\mathbf{v}' \cdot \nabla) P'_S \rangle + \gamma \langle P'_S \nabla \cdot \mathbf{v}' \rangle = f_p Q_1(\mathbf{r}), \end{aligned} \quad (11)$$

$$\frac{\partial N_I}{\partial t} + \nabla \cdot (N_I \mathbf{v}) = q_{\text{ex1}} + q_{\text{ph}}, \quad (12)$$

$$\begin{aligned} \frac{\partial P_I}{\partial t} + (\mathbf{v} \cdot \nabla) P_I + \frac{5}{3} P_I \nabla \cdot \mathbf{v} + \langle (\mathbf{v}' \cdot \nabla) P'_I \rangle + \frac{5}{3} \langle P'_I \nabla \cdot \mathbf{v}' \rangle \\ = (q_{\text{ex1}} + q_{\text{ph}}) \frac{m_p (u^2 + \langle v'^2 \rangle)}{3} - Q_2(\mathbf{r}), \end{aligned} \quad (13)$$

$$\begin{aligned} \frac{\partial P_E}{\partial t} + (\mathbf{v} \cdot \nabla) P_E + \gamma P_E \nabla \cdot \mathbf{v} - \frac{\gamma P_E}{N_E} q_{\text{ph}} + (\gamma - 1) \\ \times \left[\frac{P_E - P_S}{\tau_{\text{SE}}} + \nabla \cdot \mathbf{q}_H \right] \\ + \langle (\mathbf{v}' \cdot \nabla) P'_E \rangle + \gamma \langle P'_E \nabla \cdot \mathbf{v}' \rangle = (1 - f_p) Q_1(\mathbf{r}), \end{aligned} \quad (14)$$

where the momentum Equation (9) is now presented in conservation form, $\mathcal{R} = \langle \rho \mathbf{v}' \mathbf{v}' - \mathbf{B}' \mathbf{B}' / 4\pi \rangle$ is the Reynolds stress tensor, $\boldsymbol{\varepsilon}_m = \langle \mathbf{v}' \times \mathbf{B}' \rangle (4\pi\rho)^{-1/2}$ is the mean turbulent electric field, and \mathbf{I} is the unit matrix. The under-bracketed terms in the above equations represent the influence of fluctuations/turbulence on the mean flow. The evolution of the terms is computed via turbulence models as described in the next section. For the electron heat flux \mathbf{q}_H we use Hollweg's "free-streaming" approximation,

$$\mathbf{q}_H = \frac{3}{2} a P_E \mathbf{v}, \quad (15)$$

where a is a constant of order unity (Hollweg 1974, 1976).

2.3. The Turbulence Transport Equations

To close the system of mean-flow Equations (8)–(14), we need a turbulence model that represents the unresolved scales of the flow while allowing computation of changes in the mean flow due to the turbulence without resolving details of the turbulent fluctuations. Although the Reynolds decomposition is not formally a scale separation, we have in mind that the stochastic components treated as fluctuations reside mainly at relatively small scales. The transport equations for turbulent quantities that we implement in this study can be written in a form similar to that used by Usmanov et al. (2012; see Appendix A for details),

$$\begin{aligned} \frac{\partial Z^2}{\partial t} = & -(\mathbf{v} \cdot \nabla)Z^2 - \frac{Z^2}{2} \nabla \cdot \mathbf{u} - \frac{2}{\rho} \mathcal{R} : \nabla \mathbf{u} + \frac{\sigma_D Z^2}{2} \nabla \cdot \mathbf{u} \\ & - \frac{m_p Z^2}{2\rho} [2(q_{\text{ex1}} + q_{\text{ex2}})(1 + \sigma_D) + q_{\text{ph}}(3 + \sigma_D)] \\ & - \frac{\alpha f^+(\sigma_c) Z^3}{\lambda} + \dot{E}_{\text{PI}}, \end{aligned} \quad (16)$$

$$\begin{aligned} \frac{\partial(Z^2 \sigma_c)}{\partial t} = & -(\mathbf{v} \cdot \nabla)(Z^2 \sigma_c) - 2\epsilon_m \cdot (\nabla \times \mathbf{u}) \\ & - \frac{Z^2 \sigma_c}{2} \left\{ \nabla \cdot \mathbf{u} + \frac{[2(q_{\text{ex1}} + q_{\text{ex2}}) + 3q_{\text{ph}}]m_p}{\rho} \right\} - \frac{\alpha f^-(\sigma_c) Z^3}{\lambda}, \end{aligned} \quad (17)$$

$$\frac{\partial \lambda}{\partial t} = -(\mathbf{v} \cdot \nabla)\lambda + \beta f^+(\sigma_c)Z - \frac{\beta \dot{E}_{\text{PI}}}{\alpha Z^2} \lambda. \quad (18)$$

The three statistical descriptors of turbulence that we treat as dependent variables in the above equations are: $Z^2 = \langle v'^2 + b'^2 \rangle$, which is twice the fluctuation energy per unit mass where $\mathbf{b}' = \mathbf{B}'(4\pi\rho)^{-1/2}$, $\sigma_c = 2\langle \mathbf{v}' \cdot \mathbf{b}' \rangle / Z^2$, which is the normalized cross helicity or cross correlation between velocity and magnetic field fluctuations, and λ , which is the correlation length. Other notations are: $\sigma_D = \langle v'^2 - b'^2 \rangle / Z^2$ is the normalized energy difference that we continue treating as a constant parameter derived from observations, α and β are the Kármán–Taylor constants (see Breech et al. 2008), and $f^\pm(\sigma_c) = (1 - \sigma_c^2)^{1/2} [(1 + \sigma_c)^{1/2} \pm (1 - \sigma_c)^{1/2}] / 2$ is a function of only σ_c (see Matthaeus et al. 2004).

The last two terms in the right-hand side of Equation (16) represent the currently adopted phenomenological models for the deposition rates of the turbulence energy into the internal energy and the turbulence energy supplied by pickup protons (see Breech et al. 2008). The energy supply/sink terms in Equations (11), (13), and (14) consequently take the form $Q_1(\mathbf{r}) = (\gamma - 1)\alpha f^+(\sigma_c)\rho Z^3/2\lambda$ and $Q_2(\mathbf{r}) = \rho \dot{E}_{\text{PI}}/3$. The energy of pickup protons transferred to solar wind protons via heating is described by a source term in the form similar to that used by Usmanov et al. (2012),

$$\dot{E}_{\text{PI}} = f_D \frac{u V_A (q_{\text{ex1}} + q_{\text{ex2}} + q_{\text{ph}})}{N_S}, \quad (19)$$

where V_A is the Alfvén speed and f_D is the efficiency factor of pickup protons in driving turbulence. The parameter f_D accounts in a crude manner for the details of the pickup proton scattering

process and in general depends on kinetic properties of the interaction between protons and waves (Smith et al. 2001; Isenberg et al. 2003; Isenberg 2005; Breech et al. 2008).

The Reynolds stresses are a driver for the turbulence energy. The energy is extracted from the mean flow (the $\nabla \cdot \mathcal{R}$ term in Equation (9)) and added to the turbulence budget where it acts as a source (the third term in the right-hand side of Equation (16), which is the double inner product of the Reynolds stress tensor and the velocity gradient tensor). It should be noted that although we retain the term “Reynolds stresses” for \mathcal{R} , in the MHD case it is actually a sum of the conventional Reynolds stresses, $\langle \rho \mathbf{v}' \mathbf{v}' \rangle$, and the turbulent Maxwell stresses, $-\langle \rho \mathbf{b}' \mathbf{b}' \rangle$. Making the assumption of structural similarity along with the assumption that the turbulence is transverse to the mean magnetic field \mathbf{B} , Usmanov et al. (2009, 2011, 2012) reduced the Reynolds stress tensor to the form

$$\frac{1}{\rho} \mathcal{R} = \frac{\sigma_D Z^2}{2} (\mathbf{I} - \hat{\mathbf{B}} \hat{\mathbf{B}}), \quad (20)$$

where $\hat{\mathbf{B}}$ is a unit vector in the direction of \mathbf{B} . This form of \mathcal{R} does not account properly for turbulence driving by large-scale velocity gradients. The absence of shear driving can be seen from the expression for the turbulence production term $-(2/\rho) \mathcal{R} : \nabla \mathbf{u}$ in Equation (16). Under the approximation (20), it takes the form $-(2/\rho) \mathcal{R} : \nabla \mathbf{u} = \sigma_D Z^2 [\hat{\mathbf{B}} \cdot (\hat{\mathbf{B}} \cdot \nabla) \mathbf{u} - \nabla \cdot \mathbf{u}]$. In the constant-velocity one-dimensional (radial) case of Breech et al. (2008), the combination of the two terms in the right-hand side of Equation (16)

$$- \frac{2}{\rho} \mathcal{R} : \nabla \mathbf{u} + \frac{\sigma_D Z^2}{2} \nabla \cdot \mathbf{u} = \sigma_D Z^2 \left[\hat{\mathbf{B}} \cdot (\hat{\mathbf{B}} \cdot \nabla) \mathbf{u} - \frac{\nabla \cdot \mathbf{u}}{2} \right] \quad (21)$$

reduces to $-M \sigma_D Z^2 u_r / r$, where $M = \cos^2 \psi$ relates to the underlying turbulence symmetry and ψ is the angle between \mathbf{B} and the radial direction. In the terminology of Breech et al. (2008), Equation (21) is the “mixing” term that accounts for mixing outgoing and incoming Alfvénic fluctuations and expansion effects. Meanwhile, the effect of shear driving, which was introduced by Breech et al. (2008) into their one-dimensional model in an ad hoc manner, is missing in Equation (16) in the case Equation (20) is valid. In addition to using the oversimplified form of the Reynolds stress tensor (20), the mean turbulent electric field ϵ_m was neglected in Usmanov et al. (2009, 2011, 2012). In the present paper, we replace Equation (20) with an eddy viscosity approximation and take into account ϵ_m as described in the next section. We note here that the derivation of Equations (16) and (17) described in the Appendix A does not involve the structural similarity assumption that was employed by Breech et al. (2008) and subsequently by Usmanov et al. (2009, 2011, 2012). Instead we model the physics of the Reynolds stresses in a more complete way that we now describe.

2.4. The Eddy Viscosity Approximation

Boussinesq (1877) introduced the concept of eddy viscosity by writing the Reynolds stress tensor in a form similar to the viscous–stress tensor in laminar flow. The eddy velocity closure relates the Reynolds stresses to the mean velocity gradients and eddy (turbulent) viscosity. An extension of the Boussinesq hypothesis to the MHD case can be written as (Yoshizawa 1998; Biskamp 2008; Yokoi et al. 2008)

$$\frac{1}{\rho} \mathcal{R} = \frac{2}{3} K_R \mathbf{I} - \nu_K \mathcal{S} + \nu_M \mathcal{M}, \quad (22)$$

where ν_K and ν_M are (kinematic) eddy viscosity coefficients, $K_R = \langle v'^2 - b'^2 \rangle / 2 = \sigma_D Z^2 / 2$ is the residual energy, and \mathcal{S} and \mathcal{M} are the strain rates of the mean velocity \mathbf{u} and the mean Alfvén velocity $\mathbf{V}_A = \mathbf{B}(4\pi\rho)^{-1/2}$, respectively. \mathcal{S} and \mathcal{M} are deviatoric (traceless) symmetric tensors given by

$$\mathcal{S} = \nabla \mathbf{u} + \nabla \mathbf{u}^T - \frac{2}{3}(\nabla \cdot \mathbf{u})\mathbf{I}, \quad \mathcal{M} = \nabla \mathbf{V}_A + \nabla \mathbf{V}_A^T - \frac{2}{3}(\nabla \cdot \mathbf{V}_A)\mathbf{I}, \quad (23)$$

where the superscript T denotes the matrix transpose operation. The diagonal components of the Reynolds stress tensor (22) are normal stresses and the off-diagonal components are shear stresses. It is easy to see that in the absence of shear stresses, the left-hand side of Equation (21) gives $-\sigma_D Z^2 \nabla \cdot \mathbf{u} / 6$ and in the one-dimensional case of Breech et al. (2008) reduces to $-M\sigma_D Z^2 u_r / r$, where $M = 1/3$. In the terminology of Breech et al. (2008), it is the mixing term in the case of isotropic turbulence.

In the present study, we employ the approximation (22) and the results from the TSDIA of Yoshizawa (1984, 1998). It is a statistical method for inhomogeneous turbulence that combines a two-scale analysis with the direct-interaction approximation of Kraichnan (1964; see also, e.g., Leslie 1973). The theory relates the turbulent transport coefficients in Equation (22), which are determined by the properties of turbulence and, in general, are spatially and temporally inhomogeneous, to those in the approximation for the mean turbulent electric field,

$$\boldsymbol{\epsilon}_m = \bar{\alpha}\mathbf{B} - \bar{\beta}\nabla \times \mathbf{V}_A + \bar{\gamma}\nabla \times \mathbf{v}, \quad (24)$$

as $\nu_K = (7/5)\bar{\beta}$ and $\nu_M = (7/5)\bar{\gamma}$. The coefficients $\bar{\beta}$ (the turbulent resistivity or magnetic resistivity) and $\bar{\gamma}$ are modeled in TSDIA as $\bar{\beta} = C_\beta K^2 / \varepsilon$ and $\bar{\gamma} = C_\gamma K W / \varepsilon$, where $K = \langle v'^2 + b'^2 \rangle / 2 = Z^2 / 2$ is the energy of turbulence per unit mass, and $W = \langle \mathbf{v}' \cdot \mathbf{b}' \rangle = \sigma_c Z^2 / 2$ is the cross helicity. The model constants are estimated by Yoshizawa (1998) as $C_\beta \approx 0.05$ and $C_\gamma \approx 0.04$. The mean turbulent energy dissipation rate ε can be approximated as (see Appendix B for details)

$$\varepsilon = \frac{2C_\varepsilon}{9\sqrt{3}} \frac{Z^3}{\lambda}, \quad (25)$$

where C_ε is the dimensionless energy dissipation rate. Pearson et al. (2004) showed that in the case of stationary and isotropic hydrodynamic turbulence, C_ε , approaches the constant value of ≈ 0.5 for Reynolds numbers $\gtrsim 100$. The eddy viscosity coefficients can be expressed then as

$$\nu_K = \frac{63\sqrt{3}}{40} \frac{C_\beta}{C_\varepsilon} Z\lambda, \quad \nu_M = \frac{63\sqrt{3}}{40} \frac{C_\gamma}{C_\varepsilon} \sigma_c Z\lambda, \quad (26)$$

or approximately $\nu_K \approx 0.27Z\lambda$ and $\nu_M \approx 0.22\sigma_c Z\lambda$. Note that the sign of ν_M is determined by the sign of σ_c , which in turn depends on whether the radial magnetic field B_r is positive (directed away from the Sun) or negative (directed toward the Sun); the sign of the $\nu_M \mathcal{M}$ and $-\bar{\beta}\nabla \times \mathbf{V}_A$ terms in Equations (22) and (24) is however independent of the sign of B_r .

It should be noted that Equations (22) and (24) have been formulated by Yoshizawa (1998) under the assumption of a constant mean density ρ . Yokoi (2013) and Yokoi et al. (2013) argue that the equations are still valid in the case of non-uniform mean density if the density fluctuations are neglected ($\rho' = 0$). We will neglect the first term in Equation (24) as the study by

Marsch & Tu (1992) based on *Helios* data suggests that the α -effect in the solar wind is negligible. We do not include a higher-order (in the TSDIA formalism) frame-rotation related term in Equation (22) (see Yoshizawa 1998) assuming that its effect is relatively small. Meanwhile, the frame rotation is taken into account in Equation (24), which contains the mean vorticity in the rotating frame $\nabla \times \mathbf{v} (= \nabla \times \mathbf{u} + 2\boldsymbol{\Omega})$.

2.5. The Governing System of Equations

To solve for the mean-flow and turbulence variables simultaneously, we combine the mean-flow Equations (8)–(14) and the turbulence transport Equations (16)–(18) into an integrated system of time-dependent equations. Assuming that the turbulence is locally incompressible, we will neglect additionally all pressure fluctuations ($P'_S = P'_E = P'_I = 0$). We can re-write then the coupled system in the following quasi-conservation form (see Appendix B in Usmanov et al. 2012 for transforming the momentum and pressure equations):

$$\frac{\partial \mathbf{W}}{\partial t} + \nabla \cdot \mathbf{F} = \mathbf{S}, \quad (27)$$

where \mathbf{W} , \mathbf{F} , and \mathbf{S} are the vectors given by

$$\mathbf{W} = (N_S, \rho \mathbf{u}, \mathbf{B}, P_S^{1/\gamma}, Z^2, Z^2 \sigma_c, \rho \lambda, N_I, P_I^{3/5}, P_E^{1/\gamma_1})^T, \quad (28)$$

$$\mathbf{F} = S_h \begin{pmatrix} N_S \mathbf{v} \\ \rho \mathbf{v} \mathbf{u} - \mathbf{B} \mathbf{B} / 4\pi + \bar{P} \mathbf{I} + \mathcal{R} \\ \mathbf{v} \mathbf{B} - \mathbf{B} \mathbf{v} \\ P_S^{1/\gamma} \mathbf{v} \\ Z^2 \mathbf{v} \\ Z^2 \sigma_c \mathbf{v} \\ \rho \lambda \mathbf{v} \\ N_I \mathbf{v} \\ P_I^{3/5} \mathbf{v} \\ P_E^{1/\gamma_1} \mathbf{v} (\gamma - 1) / (\gamma_1 - 1) \end{pmatrix}, \quad (29)$$

$$\mathbf{S} = \begin{pmatrix} -q_{\text{ex}1} \\ -(q_{\text{ex}1} + q_{\text{ex}2})\mathbf{u} - \rho \left(\frac{GM_\odot}{r^2} \mathbf{r} + \boldsymbol{\Omega} \times \mathbf{u} \right) \\ \nabla \times (\sqrt{4\pi\rho} \boldsymbol{\epsilon}_m) \\ -\frac{P_S^{1/\gamma}}{\gamma} \left\{ \frac{\gamma q_{\text{ex}1}}{\rho_S} + (\gamma - 1) \left[\frac{P_S - P_E}{P_S \tau_{SE}} - f_p \frac{\alpha f^+(\sigma_c) \rho Z^3}{2\lambda P_S} \right] \right\} \\ \frac{Z^2}{2} \left\{ (1 + \sigma_D) \nabla \cdot \mathbf{u} - \frac{1}{\rho} [2(q_{\text{ex}1} + q_{\text{ex}2})(\sigma_D + 1) + q_{\text{ph}}(\sigma_D + 3)] \right\} \\ -\frac{2}{\gamma} \mathcal{R} : \nabla \mathbf{u} - \frac{\alpha f^+(\sigma_c) Z^3}{\lambda} + \dot{E}_{\text{PI}} \\ \frac{Z^2 \sigma_c}{2} \left[\frac{\rho}{\nabla \cdot \mathbf{u}} - \frac{2(q_{\text{ex}1} + q_{\text{ex}2}) + 3q_{\text{ph}}}{\rho} \right] - 2\boldsymbol{\epsilon}_m \cdot (\nabla \times \mathbf{u}) - \frac{\alpha f^-(\sigma_c) Z^3}{\lambda} \\ \rho \beta \left[f^+(\sigma_c) Z - \frac{\lambda \dot{E}_{\text{PI}}}{\alpha Z^2} \right] + q_{\text{ph}} \lambda \\ \frac{q_{\text{ex}1} + q_{\text{ph}}}{1} \left\{ (q_{\text{ex}1} + q_{\text{ph}}) \left[u^2 + \frac{1 + \sigma_D}{2} Z^2 \right] - \rho \dot{E}_{\text{PI}} \right\} \\ \frac{5P_I^{2/5} E_u}{P_E^{1/\gamma_1}} \left\{ -\frac{\gamma q_{\text{ph}}}{\rho} + (\gamma - 1) \left[\frac{P_E - P_S}{P_E \tau_{SE}} - (1 - f_p) \frac{\alpha f^+(\sigma_c) \rho Z^3}{2\lambda P_E} \right] \right\} \end{pmatrix}, \quad (30)$$

and the total pressure

$$\bar{P} = P_S + P_E + P_I + \frac{(1 + \sigma_D) \rho Z^2}{4} + \frac{B^2}{8\pi}.$$

The effective polytropic index

$$\gamma_1 = \frac{\gamma + (3a/2)(\gamma - 1)}{1 + (3a/2)(\gamma - 1)}$$

depends on Hollweg’s constant a (Jacques 1978; Meyer-Vernet 2007; Usmanov et al. 2012); for example, if $\gamma = 5/3$ and $a = 1$ then $\gamma_1 = 1.33$. For the Reynolds stress tensor \mathcal{R} defined by Equation (22), it is easy to show that the turbulence production term takes the form

$$-\frac{2}{\rho}\mathcal{R}:\nabla\mathbf{u} = -\frac{2}{3}\sigma_D Z^2 \nabla\cdot\mathbf{u} + \nu_K \mathcal{S}:\mathcal{S} - \nu_M \mathcal{S}:\mathcal{M}.$$

Following Whang (2010), the production rates of pickup protons from interstellar hydrogen atoms by charge exchange with solar wind protons and with interstellar pickup protons, and by photoionization are taken as $q_{\text{ex1}} = \sigma N_H N_S u$, $q_{\text{ex2}} = \sigma N_I N_S u$, and $q_{\text{ph}} = \nu_0 (r_0^2/r^2) N_H$, respectively. N_H is the number density of the interstellar hydrogen, $\sigma = (7.6 \times 10^{-8} - 1.06 \times 10^{-8} \log E)^2 \text{ cm}^2$ is the mean charge exchange cross section of hydrogen atoms (Fite et al. 1962), where the proton energy E (in eV) $= [V \text{ (in cm s}^{-1})/1.384]^2 \times 10^{-12}$, and $\nu_0 = 0.9 \times 10^{-7} \text{ s}^{-1}$ is the rate of photoionization per hydrogen atom at the heliocentric distance $r_0 = 1 \text{ AU}$. The density distribution of interstellar hydrogen is assumed to have the form (Breech et al. 2008)

$$N_H = N_{H0} \exp\left(-\frac{L_{\text{cav}}}{r}\right),$$

where N_{H0} is the number density of interstellar hydrogen at the termination shock and L_{cav} is the characteristic radius of the ionization cavity around the Sun.

2.6. Numerical Scheme

We construct numerical steady-state solutions of the system of equations (Equation (27)) on a composite spherical grid (Usmanov 1996; Usmanov et al. 2012) in the region from 0.3 to 100 AU by the time-relaxation method. We use the central weighted essentially non-oscillatory (CWENO) spatially third-order discretization algorithm of Kurganov & Levy (2000) combined with the strong stability-preserving Runge–Kutta time integration third-order scheme of Gottlieb et al. (2001), and the eight-wave method of Powell (1994) to maintain the $\nabla \cdot \mathbf{B} = 0$ condition. The grid resolution is similar to that used by Usmanov et al. (2012). In the axisymmetric case, 300 grid points are spaced logarithmically along the radius with the step increasing from 0.006 AU at the inner boundary of 0.3 AU to 2 AU at 100 AU. The latitudinal resolution is 1° . In the fully three-dimensional case, the computational region is divided into three subregions: 0.3–20, 20–60, and 60–100 AU, with the universal angular resolution of 1.5° and 600 equidistant points along the radial coordinate in each subregion.

2.7. Boundary and Initial Conditions

The initial and boundary conditions are similar to those described in Usmanov et al. (2012). To assign most of boundary conditions at 0.3 AU and initial conditions from 0.3 to 100 AU, we use the results from the solar corona and solar wind model (ALF3D), which is an updated fully three-dimensional version of the model of Usmanov (1996), Usmanov et al. (2000), and Usmanov & Goldstein (2003). In this model, steady-state solutions of the polytropic MHD solar wind equations in the rotating with the Sun spherical coordinates are constructed for a source magnetic field on the Sun specified either as a dipole (aligned or tilted with respect to the solar rotation axis) or as derived from synoptic solar magnetograms for

different solar rotations. The model assumes that a flux of Alfvén waves propagates away from the Sun and provides additional acceleration and heating for the solar wind flow. The MHD equations are correspondingly augmented to include a conservation equation for the Alfvén wave energy density in the WKB approximation (Jacques 1978). The computational domain in ALF3D is split into two subregions. In the inner (coronal) subregion that extends from 1 to $20 R_\odot$, where R_\odot is the radius of the Sun, the polytropic index γ is taken to be 1.08, i.e., close to the isothermal value, and a steady-state solution for transonic and trans-Alfvénic coronal outflow is obtained by a time-relaxation method, i.e., by time integration of non-stationary equations until a steady-state is achieved. The inner boundary conditions (prescribed on a sphere $r = 1 R_\odot$) depend on time in the sense that they are updated in the course of relaxation process to be consistent with the flow characteristics near the boundary (see discussion in Usmanov et al. 2000), but they evolve to a steady state simultaneously with the solution in the inner subregion. The boundary between the inner and outer subregions is chosen at $20 R_\odot$ to assure that the solar wind flow at the boundary is supersonic and super-Alfvénic. The outflow boundary conditions at $20 R_\odot$ are approximated by a first-order (linear) extrapolation. In the outer subregion from $20 R_\odot$ to 100 AU, the adiabatic index $\gamma = 5/3$ is used in combination with Hollweg’s electron heat flux (15), and a steady-state solution is constructed by means of a marching-along-radius numerical method (Pizzo 1978, 1982; Usmanov 1993).

Important improvements of the present version of ALF3D is that it implements the CWENO numerical scheme of Kurganov & Levy (2000) and, while a one-fluid plasma description is used in the inner region, the model includes separate energy equations for electrons and protons in the outer region. As a result, the thermal pressures of solar wind protons and electrons are set to be equal at the inner boundary of $20 R_\odot$. It is assumed that the Alfvén waves do not damp in the inner region, and that in the outer region, the waves are damped by a mechanism that may be characterized by a phenomenological dissipation length that we set to $20 R_\odot$. The following input parameters for ALF3D are specified at the base of solar corona: the driving amplitude of Alfvén waves (35 km s^{-1}), the initial density ($0.4 \times 10^8 \text{ particle cm}^{-3}$), and plasma temperature ($1.8 \times 10^6 \text{ K}$). The magnetic field magnitude is assigned either as the field strength of the source magnetic dipole on the Sun’s poles (the strength was chosen to be 16 G to match magnitude of the heliospheric magnetic field observed by *Ulysses*; see Section 3.4) or from the line-of-site observations of the photospheric magnetic field at the Wilcox Solar Observatory.

Figure 1 illustrates the boundary conditions prescribed at 0.3 AU in the axisymmetric case. Most of the profiles are extracted from an ALF3D solution for a source magnetic dipole on the Sun aligned with the solar rotation axis. The exceptions are the variations of the cross helicity σ_c and the correlation length λ , which are set up to vary as $\sigma_c = -\sigma_{c0} B_r / |B_r^{\text{max}}|$ and $\lambda = \lambda_0 u_r / u_r^{\text{max}}$, where B_r^{max} and u_r^{max} are the maximum values of B_r and u_r at 0.3 AU and the values of σ_{c0} and λ_0 are taken to be 0.8 and 0.01 AU, respectively. The distribution of Z^2 at the boundary is calculated from the WKB Alfvén wave energy density \mathcal{E} provided by ALF3D as $Z^2 = 2\mathcal{E}/\rho$. The number proton density and temperature of pickup protons at 0.3 AU are chosen to be $N_I = 1.0 \times 10^{-5} \text{ cm}^{-3}$ and $T_I = 10^6 \text{ K}$ (we found that the simulation results beyond $\sim 1 \text{ AU}$ were insensitive to the values of N_I and T_I at the inner boundary in agreement

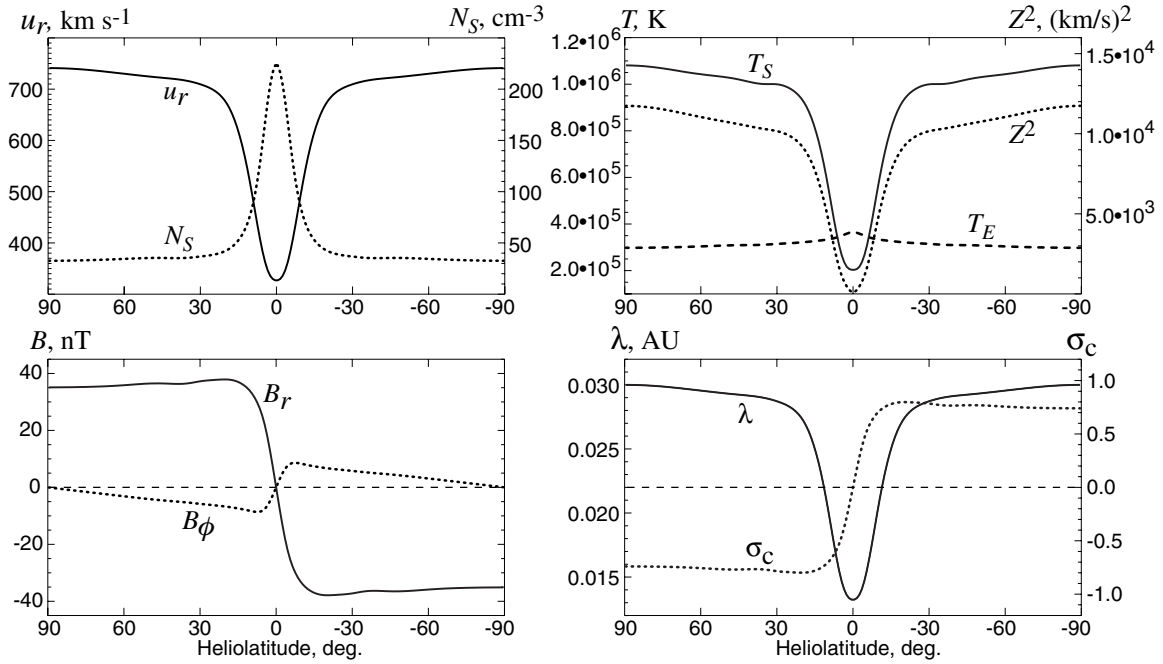


Figure 1. Boundary conditions for plasma, magnetic field, and turbulence quantities in the axisymmetric case at 0.3 AU as a function of heliolatitude.

with the similar result of Isenberg (1986). The fast solar wind velocity decreases slowly with latitude from the pole toward the equator before undergoing a steep transition from $\sim 700 \text{ km s}^{-1}$ to $\sim 330 \text{ km s}^{-1}$ within $\sim 20^\circ$ of latitude. The density variation is inverse to that of velocity with a maximum on the equator in the slow wind. The profiles of proton temperature T_S , turbulence energy Z^2 , and the correlation length λ are similar to the u_r profile. Meantime, the electron temperature instead slightly increases toward the equator. The radial magnetic field B_r is relatively constant in the fast wind, while the azimuthal field B_ϕ increases linearly toward the equator. Both components change sign in the slow solar wind near the equator.

2.8. Model Parameters

Following Breech et al. (2008, 2009), we use the following values for the normalized energy difference $\sigma_D = -1/3$, the isotropization parameter that relates to the fraction of pickup proton kinetic energy transferred into waves through the isotropization process $f_D = 0.25$, the number density of interstellar hydrogen at the termination shock $N_{H0} = 0.1 \text{ cm}^{-3}$, the characteristic radius of the ionization cavity around the Sun $L_{\text{cav}} = 8 \text{ AU}$, the fraction of turbulent energy absorbed by protons $f_p = 0.6$, and the proton–electron collision time scale $\tau_{SE} = 2 \times 10^6 \text{ s}$. We set the polytropic index to the adiabatic value $\gamma = 5/3$ and assume that solar wind heating comes from the turbulent cascade and the electron heat flux. For the constant a in Hollweg’s electron heat flux model (15) we use the value $a = 1.05$. As was demonstrated by Cranmer et al. (2009), Hollweg’s formula with $a = 1.05$ fits closely *Helios* (Pilipp et al. 1990) and *Ulysses* (Scime et al. 1999) observations.

It is shown in Appendix B that the Kármán–Taylor constant α is related to the non-dimensional mean turbulent energy dissipation rate, C_ε , as $\alpha = 4C_\varepsilon/9\sqrt{3}$. We use the value of $C_\varepsilon = 0.5$ that was obtained by Pearson et al. (2004) based on their simulation results in the hydrodynamic case, which corresponds to $\alpha = 0.128$. Note that this α is notably smaller than the one (0.8) used by Breech et al. (2008). Breech et al.

(2009) used $\alpha = 0.5$, while even smaller $\alpha = 0.25$ and 0.125 worked well in a model that computes cosmic ray mean free paths (Pei et al. 2010). Following Breech et al. (2008, 2009), we continue to employ the relation between the Kármán–Taylor constants $\alpha = 2\beta$ that for our choice of α gives $\beta = 0.064$.

3. SIMULATION RESULTS

3.1. Axially Symmetric Case

Figure 2 shows a steady-state solution of the system of equations (Equation (27)) in the meridional plane as contour plots of the mean-flow and turbulent quantities for a source magnetic dipole on the Sun aligned with the solar rotation axis. In this case, the solution is axially symmetric about the axis, fast and slow wind streams do not become radially aligned, and the corotating interaction regions therefore do not form. The integration time for this solution to reach the steady state was 16,000 hr or $\sim 1.8 \text{ yr}$. Although the range of heliocentric distances is from 0.3 to 100 AU, recall that this model is applicable only to the supersonic and super-Alfvénic solar wind and it does not describe the solar wind interaction with the local interstellar medium and, as a result, does not include any of the heliospheric interface boundaries (the termination shock, heliopause or bow shock). In general, the results in Figure 2 are similar to those in Figure 3 in Usmanov et al. (2012) in showing the bimodal solar wind with slower and denser wind near the equator and more tenuous and faster wind at higher latitudes. The deceleration of the wind due to its interaction with the interstellar hydrogen through charge exchange and photoionization is clearly seen in Figure 2(a) beyond the slow velocity band near the equator. The magnetic field magnitude B is relatively small near the pole, where B_ϕ is negligible in comparison with B_r decreasing as r^{-2} , and near the equator, where $B = 0$ due to the assumed north–south symmetry of the problem. Unlike Figure 3 in Usmanov et al. (2012), Figure 2 shows separate distributions for the solar proton and electron temperatures (Figures 2(d) and (e)).

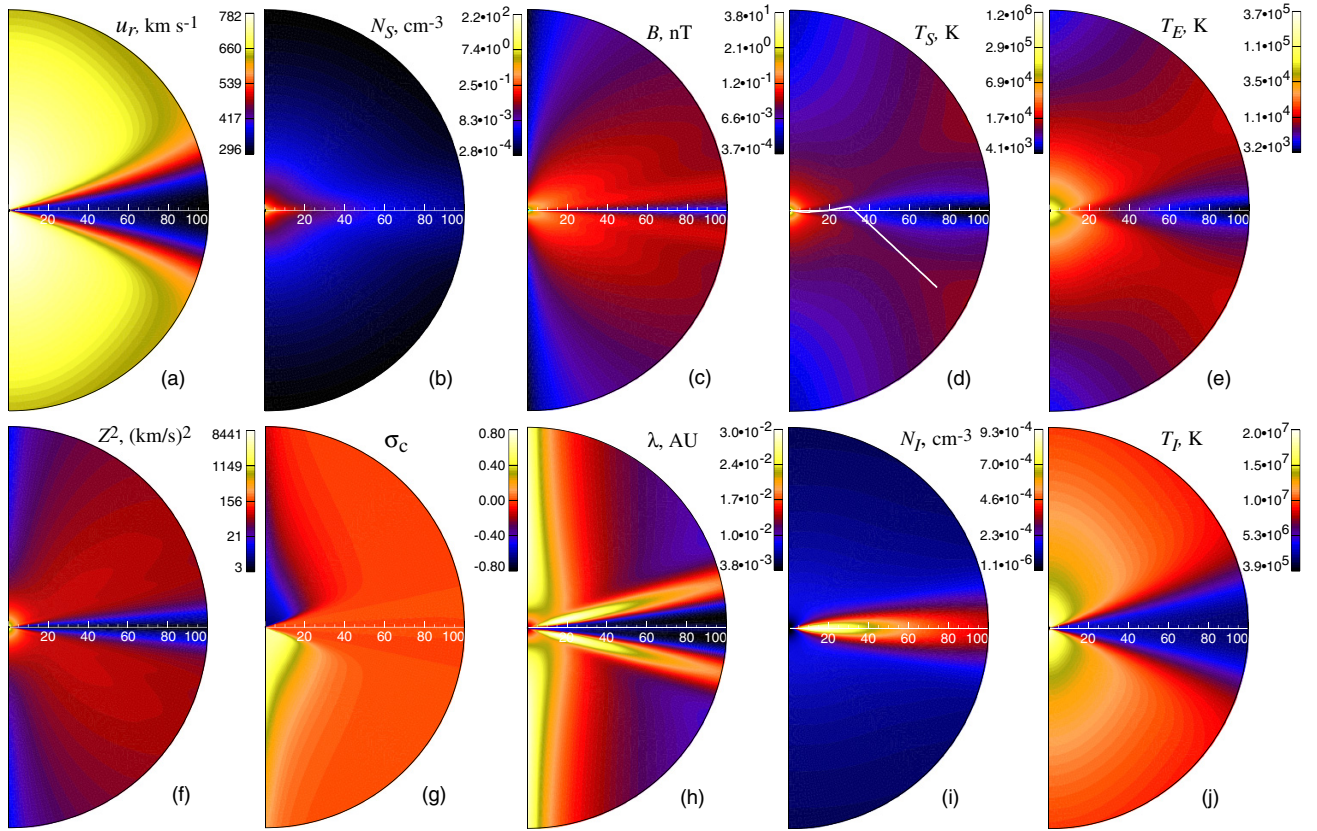


Figure 2. Contour plots of the computed parameters in the meridional plane from 0.3 to 100 AU for the axisymmetric case of a magnetic dipole on the Sun aligned with the solar rotation axis: (a) the radial velocity u_r , (b) the number density of solar wind protons N_S , (c) the magnetic field magnitude B , (d) the temperature of solar wind protons T_S , (e) the temperature of electrons T_E , (f) the turbulence energy Z^2 , (g) the normalized cross helicity σ_c , (h) the correlation length scale λ , (i) the number density N_I , and (j) the temperature T_I of pickup protons. The white line in the T_S plot (d) depicts the projection of the *Voyager 2* trajectory on the meridional plane. (A color version of this figure is available in the online journal.)

3.2. The Effect of Coulomb Collisions

To demonstrate the role of Coulomb collisions between the solar wind protons and electrons, Figure 3 compares the radial profiles of the temperatures computed with the axisymmetric model at the heliolatitude of 30.5° for the collision time scale $\tau_{SE} = 2 \times 10^6$ s, which approximately corresponds to the solar wind transit time to 10 AU (Breech et al. 2009), and for the case in which all the collisional terms in the energy equations for solar wind protons and electrons are turned off ($\tau_{SE} = \infty$). One can see from Figure 3(b) that in the absence of Coulomb collisions, even though T_E is ~ 3 times smaller than T_S near the inner boundary, T_E significantly (up to 4 times) exceeds T_S throughout the rest of computational domain. The dominance of T_E is obviously a result of the electron heat conduction. The presence of collisions (the upper plot) changes the situation dramatically: T_S is now close to and even slightly exceeds T_E beyond ~ 40 AU. Therefore, even extremely rare collisions with a mean free path of order 10 AU can redistribute the thermal energy between solar wind protons and electrons substantially. The temperature of pickup protons, T_I , is practically unaffected by the presence or absence of Coulomb collisions between the solar wind protons and electrons and it is close to the estimates of the pickup proton temperature from *Voyager 2* measurements near 35, 39–41, and 43 AU by Burlaga et al. (1994, 1996).

3.3. The Effect of Eddy Viscosity

The off-diagonal elements of the Reynolds stress tensor \mathcal{R} in Equation (22) are responsible for the shearing effects and

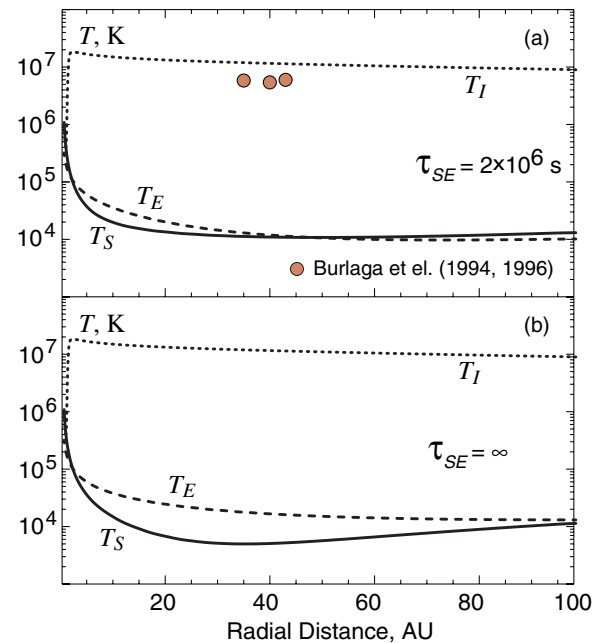


Figure 3. Solar wind proton T_S , electron T_E , and pickup proton T_I temperature profiles at latitude $+30.5^\circ$ in the axisymmetric model with (a) and without (b) Coulomb collisions between solar wind protons and electrons. The small circles represent the values of T_I inferred from *Voyager 2* observations of pressure-balanced structures by Burlaga et al. (1994, 1996). (A color version of this figure is available in the online journal.)

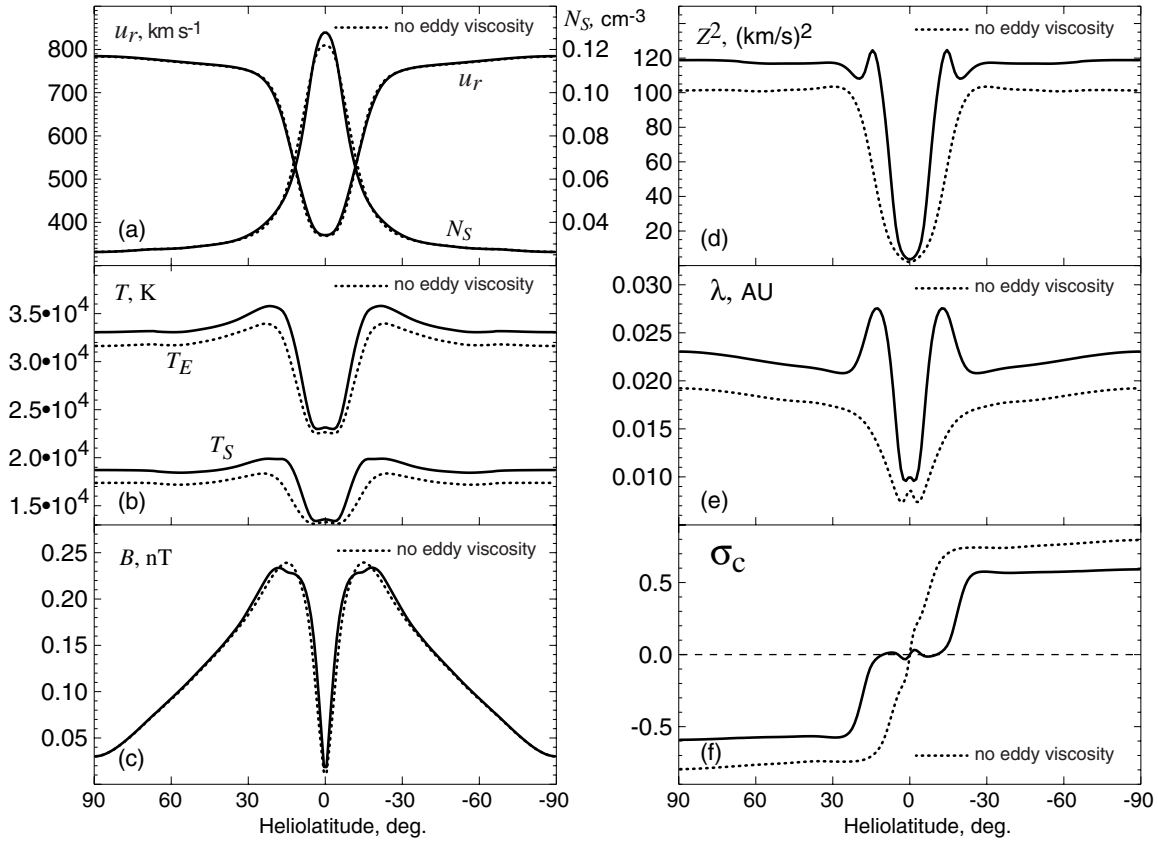


Figure 4. Latitudinal profiles at $r = 10$ AU in the axisymmetric model of the computed radial velocity u_r and solar proton density N_S (a), solar proton T_S and electron T_E temperatures (b), magnetic field magnitude B (c), turbulence energy Z^2 (d), correlation length λ (e), and cross helicity σ_c (f). The dotted curves depict the model results with the eddy viscosity turned off.

increase of the turbulence energy. To evaluate the influence of eddy viscosity and, correspondingly, of shear driving on the plasma and turbulence parameters, Figure 4 compares latitudinal profiles of the parameters computed at 10 AU with the eddy viscosity turned on and off ($\nu_K = \nu_M = 0$). The radial velocity u_r and solar proton density N_S profiles are only slightly different in both cases, while the effect of shear driving is clearly seen in the solar proton T_S and electron T_E temperatures, which show additional heating if the eddy viscosity is on, and in the turbulence quantities. The turbulence energy Z^2 and the correlation length λ are both increased and the cross helicity σ_c is correspondingly decreased. As one might expect, the effect of eddy viscosity is most prominent at the transition between fast and slow wind, i.e., in the regions of high shear. The effect of shearing in the presence of corotating interaction region can be seen in Figure 5 that shows the latitudinal profiles of the same variables as in Figure 4, but in the model with the solar dipole tilted by 10° . The profiles are now asymmetric with respect to the equator and show a compression (rarefaction) at the northern (southern) transition between fast and slow wind. The effect of shearing is particularly evident within the compression region where Z^2 and λ are sharply increased.

The effect of shear driving on the cross helicity, which is already seen in Figure 4, is demonstrated in Figure 6 by contour plots of σ_c in the meridional plane. The figure compares the distributions of cross helicity in the meridional plane for the cases with the eddy viscosity on (panel (a)) and off (panel (b)). The interval of heliocentric distances in Figure 6 was intentionally restricted to the region from 0.3 to 10 AU,

where the pickup proton effects are relatively small and are overwhelmed by the shear driving. One can see from Figure 6(a) that σ_c is near zero within the range of latitudes approx. $\pm 20^\circ$ that closely corresponds to the region of large meridional gradients (high shear) in the radial velocity (Figure 6(c)). In contrast, σ_c in Figure 6(b), which shows the case with the eddy viscosity turned off, is suppressed in a much narrow region near the equator.

Figure 7 shows latitudinal profiles of the eddy viscosity coefficients ν_K and ν_M at 1 AU. The coefficients only slightly vary with latitude in the fast solar wind and sharply decrease toward the equator in the slow wind. The fast wind values of the coefficients are $\nu_K \approx 2 \times 10^{17} \text{ cm}^2 \text{ s}^{-1}$ and $\nu_M \approx 10^{17} \text{ cm}^2 \text{ s}^{-1}$. The value of ν_K is close to the estimate of $1.3 \times 10^{17} \text{ cm}^2 \text{ s}^{-1}$ by Borovsky (2006), who used an expression for ν_K similar to Equation (26). It should be noted that the estimate of Borovsky (2006) is based on the observed amplitudes of velocity and magnetic field fluctuations at Earth's orbit, i.e., near the helioequatorial plane where the solar wind is typically slow during both solar minimum and maximum. It follows from our simulation, that ν_K in the slow wind can be about an order of magnitude smaller than the one in the fast wind, while the difference for ν_M can reach two orders of magnitude.

Although the effect of the eddy viscosity on the mean flow parameters is not dramatic and mostly leads to higher temperatures, the turbulence energy is significantly increased at the fast-slow stream interfaces and the correlation length is correspondingly increased. This is the obvious result of shear driving at the large-scale velocity gradients.

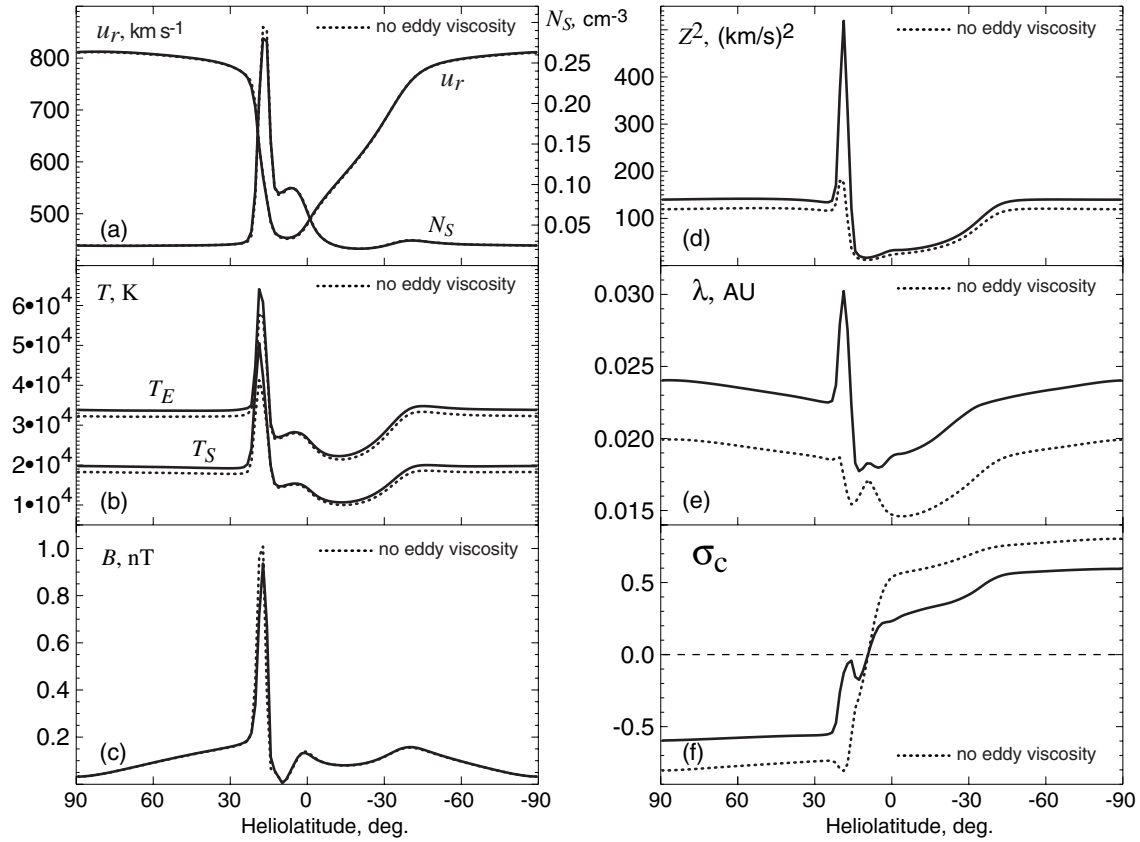


Figure 5. Latitudinal profiles at $r = 10$ AU and $\phi = 0.75$ of the same variables as in Figure 4, but for the source dipole on the Sun tilted by 10° . The dotted curves depict the model results with the eddy viscosity turned off.

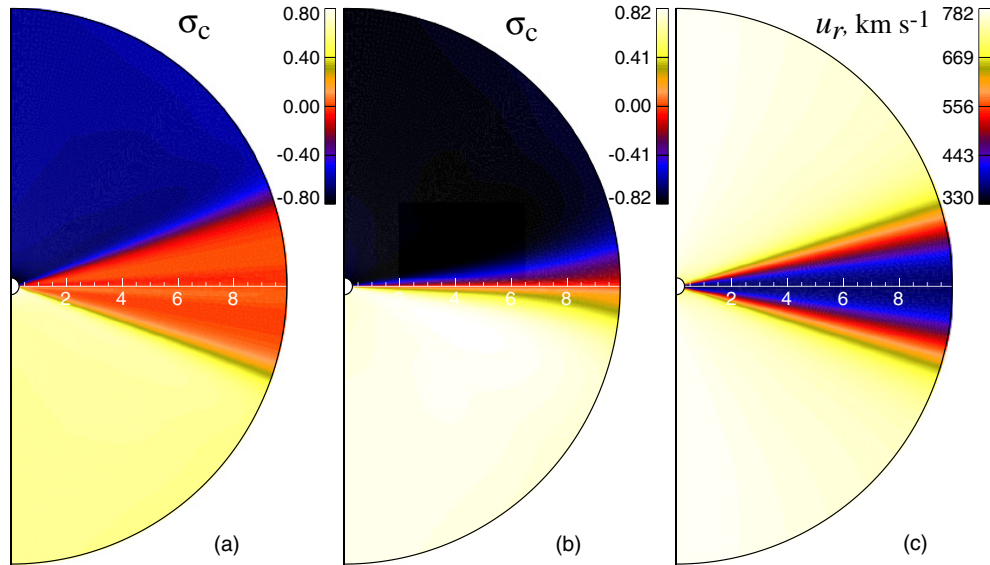


Figure 6. Contour plots in the meridional plane from 0.3 to 10 AU of the cross helicity σ_c in the axisymmetric model with the eddy viscosity turned on (a) and off (b), and of the radial velocity u_r (c).

(A color version of this figure is available in the online journal.)

3.4. Comparison with *Ulysses*

Figure 8 compares *Ulysses* observations with the model results for a source dipole on the Sun tilted by 10° . This value of the tilt is approximately consistent with the distribution of solar magnetic field during *Ulysses*' first fast scan in latitude from -80° to $+80^\circ$ in 1994–1995 (Usmanov & Goldstein 2003). In

contrast to the comparison of the *Ulysses* data with an earlier version of the model in Usmanov et al. (2011), Figure 8 shows separate temperatures for solar wind protons and electrons versus the *Ulysses* observations. Although the computed electron temperature is somewhat larger than the observed one, the proton temperature generally matches the “ T -small” estimate of the observed proton temperature and the general variations of all the

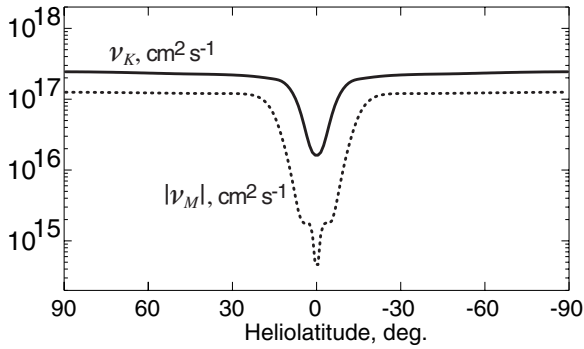


Figure 7. Latitudinal profiles of the computed eddy viscosity coefficients ν_K (solid line) and ν_M (dotted line) at 1 AU in the axisymmetric model.

plasma and magnetic field parameters are reproduced relatively well. This fact supports our belief that the boundary conditions at our inner boundary of 0.3 AU are reasonable.

3.5. Solar Corona and Solar Wind Simulation for Carrington Rotation 2123

In this section, we present simulation results for a specific solar rotation, which were obtained using a synoptic solar magnetogram to prescribe boundary conditions at the coronal base. We have selected Carrington Rotation (CR) 2123, April 28 to May 25, 2012, as a period close to the maximum of solar cy-

cle 24, which started in 2009 September. During this rotation, the distribution of magnetic field on the solar photosphere was typical for the maximum phase of a solar cycle with many bipolar active regions above and below the solar equator and with a complex neutral line extending to polar regions. Figure 9(b) shows a contour plot of the radial magnetic field B_r distribution in the heliographic coordinates, which we computed from the spherical harmonic coefficients (up to the ninth order) published by the Wilcox Solar Observatory. The expansion coefficients are routinely calculated at the Stanford University from daily solar magnetograms assuming either “line-of-sight” or “radial” boundary conditions at the photosphere. The distribution of B_r shown in Figure 9(b) covers the range from -36 to 40 G and corresponds to the “radial” conditions, which usually provide a higher range of magnitudes than the “line-of-sight” conditions. We used the B_r distribution shown in Figure 9(b) as boundary condition at the coronal base and kept it fixed in the course of relaxation.

Figure 9(a) shows the coronal magnetic field configuration for CR2123, which was computed using the ALF3D model described in Section 2.7. The plot represents a snapshot at the time $t = 32$ hr, when the plasma-magnetic field system had already reached a steady state. The field lines were traced from the coronal base on a grid with a step of 10° in latitude and longitude to the heliocentric distances up to $1.8 R_\odot$. The magnetic field lines are mostly closed loops and lonely open field lines except for a bunch of open field lines around the

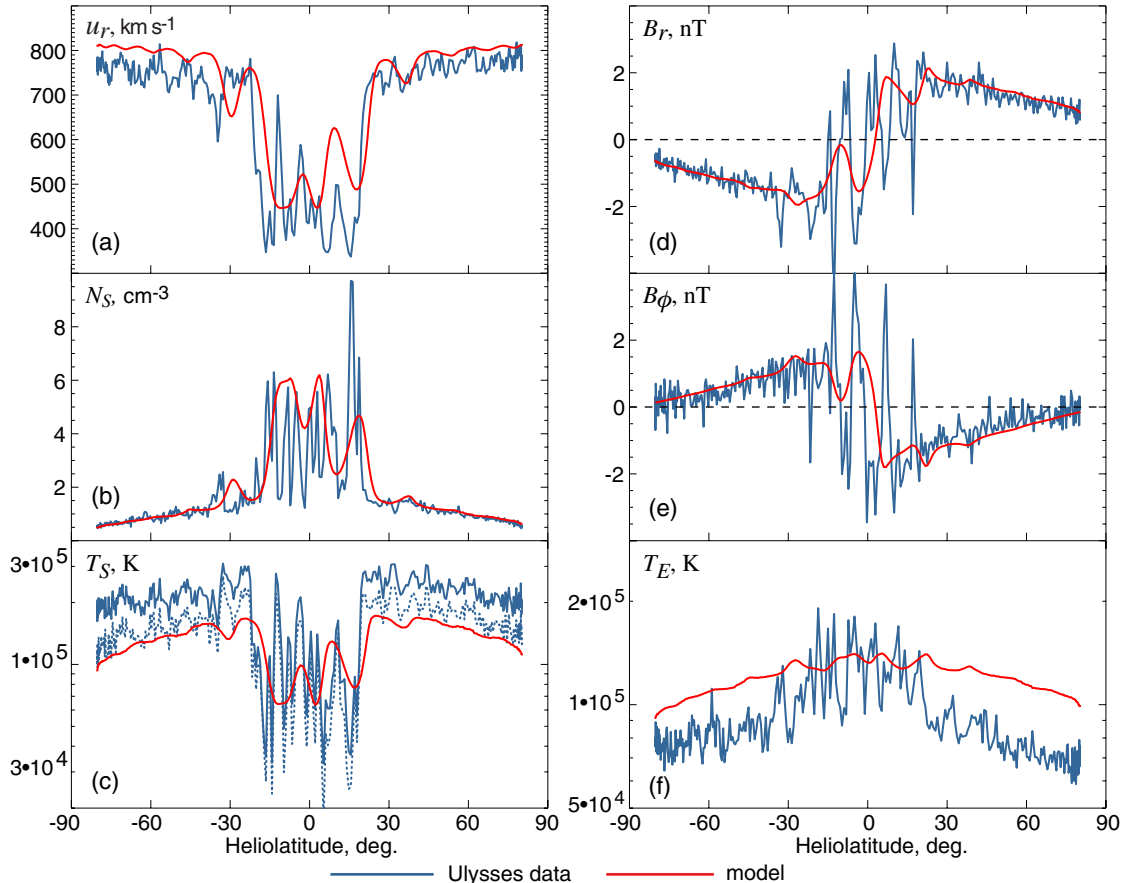


Figure 8. Simulated profiles (red) for a source magnetic dipole on the Sun tilted by 10° (with respect to the solar rotation axis) vs. *Ulysses* daily averages of plasma and magnetic field parameters measured during the first fast latitude transit of *Ulysses* in 1994–1995. The parameters shown are: the radial velocity u_r (a), the number density of solar protons N_S (b) and their temperature T_S (c), the radial B_r (d) and azimuthal B_ϕ (e) magnetic field, and the electron temperature T_E (f). Two estimates, “ T -large” and “ T -small” of the proton temperature measured by *Ulysses* are shown by blue solid and dotted lines, respectively.

(A color version of this figure is available in the online journal.)

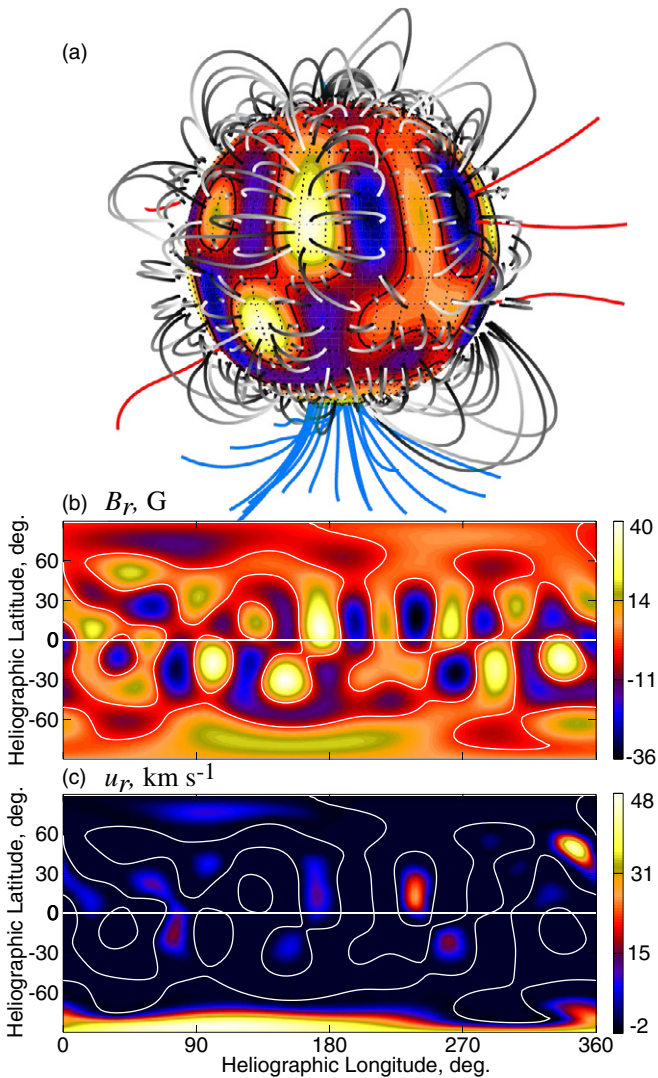


Figure 9. Results from the coronal simulation for Carrington Rotation 2123: (a) magnetic field topology in the region $1\text{--}1.8 R_\odot$; the view is from the equatorial plane at 180° of heliolongitude, corresponding to Earth’s location on 2012 May 11 at 19:25 UT; the blue (red) lines are open field lines with magnetic field directed away (toward) the Sun; the gray lines are closed field lines; (b) and (c): contour plots at $r = 1 R_\odot$ of the radial magnetic field strength, B_r (in gauss), and the radial velocity, u_r (in km s^{-1}), respectively; the white line in both plots depicts the neutral line where $B_r = 0$.

(A color version of this figure is available in the online journal.)

south pole. In the ALF3D code, the radial flow velocity at the inner boundary is not fixed, but instead is calculated from the subsonic/sub-Alfvénic flow properties near the boundary. The results for the computed u_r at the coronal base are presented in Figure 9(c). Near the coronal base, the magnetic field is strong enough to suppress plasma outflow, so u_r is close to zero through the most of coronal base except for a number of relatively small and low-speed regions north and south of the equator, and the region near the south pole, which coincides with the region of open field lines in Figure 9(a). The model results shown in Figure 9 provide boundary conditions for the solar wind module of ALF3D that was used to construct the solution by forward integration along radius from $20 R_\odot$ to 0.3 AU . Finally, the results of integration to 0.3 AU are used for setting up boundary conditions (shown in Figure 10) for the solar wind model with turbulence transport presented in this paper.

Figure 11 shows the computed solar wind flow, magnetic field, and turbulence parameters for Carrington Rotation 2123 as contour plots in the meridional plane $\phi = 0.75$. The upper 10 plots are for the region $0.3\text{--}20 \text{ AU}$ and the lower 10 are for the region $20\text{--}100 \text{ AU}$. The solar wind structure is now much more complicated than in the axisymmetric case shown in Figure 2, where the assumed azimuthal symmetry eliminated any fast–slow wind interactions due to solar rotation and the formation of the corotating interaction regions. The solar wind in Figure 11 is highly non-uniform with an alternating fast–slow flow pattern covering all latitudes. Relatively fast solar wind can now be seen only in the high latitude region around the southern pole and in the region centered on $\sim 20^\circ$ north of the helioequator. The source region of the “southern” fast flow is obviously associated with the open field configuration around the south pole seen in Figure 9 and the corresponding plasma outflow with the speed $\sim 390 \text{ km s}^{-1}$ at 0.3 AU in Figure 10. Meantime, the “northern” fast flow that gives rise to a series of corotating interaction regions originates obviously from the fast stream with the maximum speed $\sim 530 \text{ km s}^{-1}$ north of the helioequator around longitudes 220° .

3.6. Comparison with WIND

Figure 12 shows the results of simulation for Carrington Rotation 2123 along the orbit of the Earth for the basic solar wind parameters. Same parameters as observed by the *WIND* spacecraft are shown by the red lines. One can see some agreement of the trends in the observed and computed velocity, solar proton density and temperature, and radial magnetic field. In particular, the order of magnitude of plasma parameters and the four sector magnetic field structure are in general reproduced in the simulation. This fact gives us more confidence in the simulated solar wind structure further out in the heliosphere. However, the model results mostly miss a high speed stream at heliolongitudes $\leq 45^\circ$ and the computed magnetic field magnitude is significantly smaller than that observed. We have no clear explanation of why the second high speed stream is not reproduced and the computed field is so low. We can assume that the observed photospheric magnetic field values might be in need of calibration as discussed, e.g., by Zhao & Hoeksema (1995) with a correction factor for the measured magnetic field strength from 1.8 to 3.6. We did not apply any correction factor to improve the fit to the computed field to the observed one and leave that task for further study.

3.7. Comparison with Voyager 2

Figure 13 shows radial variations of radial velocity, solar proton density, and solar proton temperature observed by *Voyager 2* during its 30 yr long journey throughout the heliosphere from 1 to 84 AU , before its crossing of the termination shock in 2007 August. The dark blue curves in Figures 13(a)–(c) represent 27 day running averages of the *Voyager 2* measurements. There are two model curves computed along *Voyager 2*’s trajectory and superimposed on the *Voyager 2* data: the red one is from the run for the solar dipole tilted by 10° and the light blue one corresponds to the run for Carrington Rotation 2123. The boundary conditions at 0.3 AU for the two models differ drastically. Those for CR2123 are shown in Figure 10 and the 10° conditions are in general similar to those shown in Figure 1, provided that the latter are appropriately “tilted.”

While the tilted-dipole curve is an approximate for solar minimum conditions with fast (slow) solar wind at high (low)

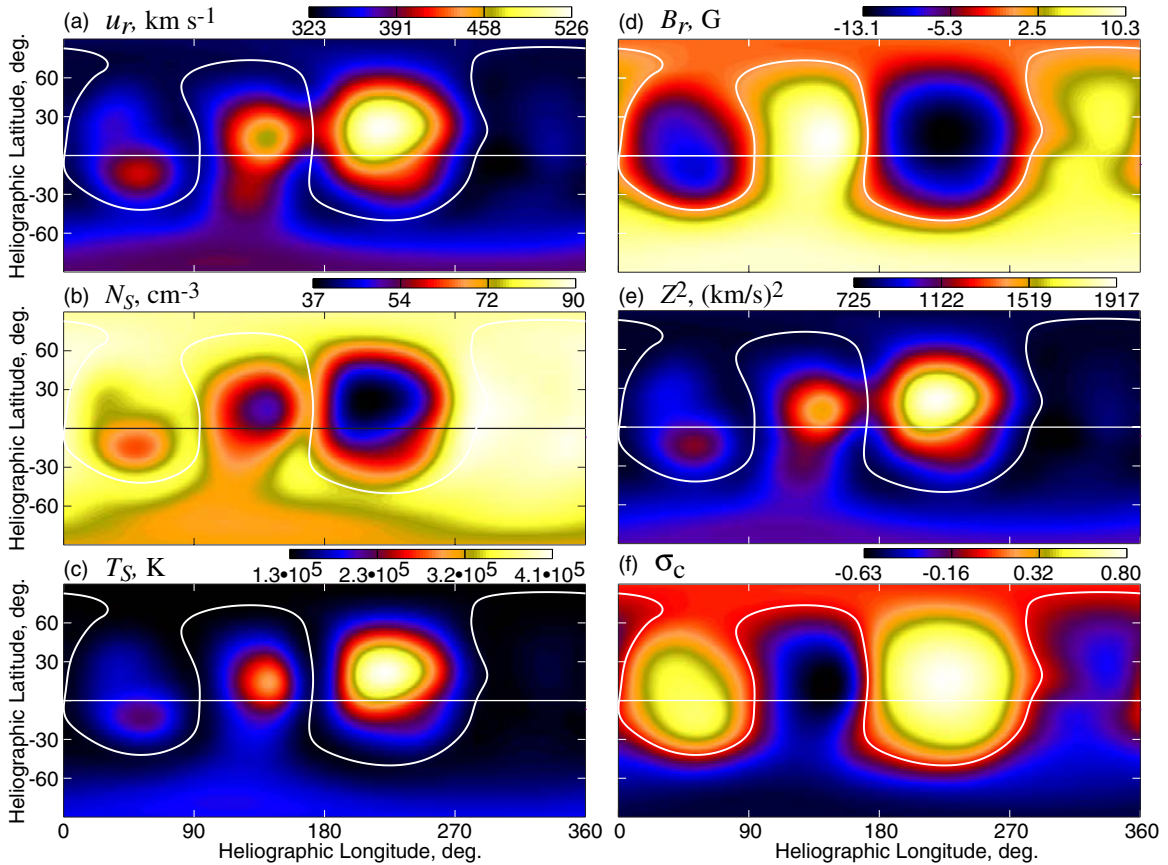


Figure 10. Boundary conditions for plasma, magnetic field and turbulence quantities at 0.3 AU for Carrington Rotation 2123. (A color version of this figure is available in the online journal.)

latitudes, the curve for CR2123 is a representative for solar maximum with slow solar wind occupying all latitudes. In general, the model profiles correspond roughly to the range of *Voyager* data that cover three solar cycles (see Figure 13(d)) with the exception of the proton temperature profile for CR2123 that goes somewhat lower than the observed values. The inflection of model profiles at ~ 35 AU in the 10° tilt case is a result of the *Voyager 2* leaving the ecliptic plane and moving toward higher southern latitudes after its encounter with Neptune in 1989 (see the spacecraft's latitude in Figure 13(d)). The effect of the latitudinal displacement of *Voyager 2* in its observations of solar wind parameters was discussed in Usmanov & Goldstein (2006). To underline the importance of Coulomb collisions between solar wind protons and electrons, Figure 13(c) shows also the profile of T_S from the 10° tilted-dipole model with the Coulomb collisions turned off. In this case, the energy gained by electrons from heat conduction is not transferred to solar wind protons and, as can be clearly seen in Figure 13(c), the computed T_S is well below the values observed by *Voyager 2*.

4. SUMMARY AND DISCUSSION

We have developed a three-fluid, fully three-dimensional MHD model of the solar wind as a co-moving system of solar wind protons, electrons, and interstellar pickup protons, with separate energy equations for each species. The model accounts for the effects of Reynolds stresses, mean turbulent electric field, pickup protons, electron heat conduction, and dissipation of turbulence on the spatial evolution of the solar wind plasma, including electron and proton temperatures, magnetic field, and turbulence. The Reynolds stresses and the mean turbulent elec-

tric field are modeled by the eddy viscosity approximation using results from the TSDIA. The coupled mean-flow Reynolds-averaged solar wind equations and turbulence transport equations written in the frame of reference corotating with the Sun are solved numerically in the region from 0.3 to 100 AU using the time-relaxation method. The model results provide three-dimensional distributions of mean-flow and turbulence parameters throughout the heliosphere for given boundary conditions at the coronal base.

Our simulations demonstrate that the effect of eddy viscosity and, correspondingly, of velocity shear on the mean-flow parameters reveals itself in the increased temperatures of solar wind protons and electrons. The turbulence energy and the correlation length are notably increased and the cross helicity decreased, especially near the transitions between fast and slow solar wind flows. The runs with and without Coulomb collisions show that the thermal energy can be substantially redistributed between solar wind protons and electrons owing to Coulomb collisions. As a result, the solar proton and electron temperatures become comparable in the outer heliosphere.

Comparisons of observed solar wind properties with those predicted by the model show a general agreement of the model results with observations on *WIND*, *Ulysses*, and *Voyager 2* spacecraft. The comparisons can serve as a test for the physical assumptions built into the model presented in this paper. The model is limited by the assumptions, most important of which are listed below.

1. Although time-dependent equations are solved, the solutions obtained by the time-relaxation method are steady-state (in the corotating with the Sun frame of reference).

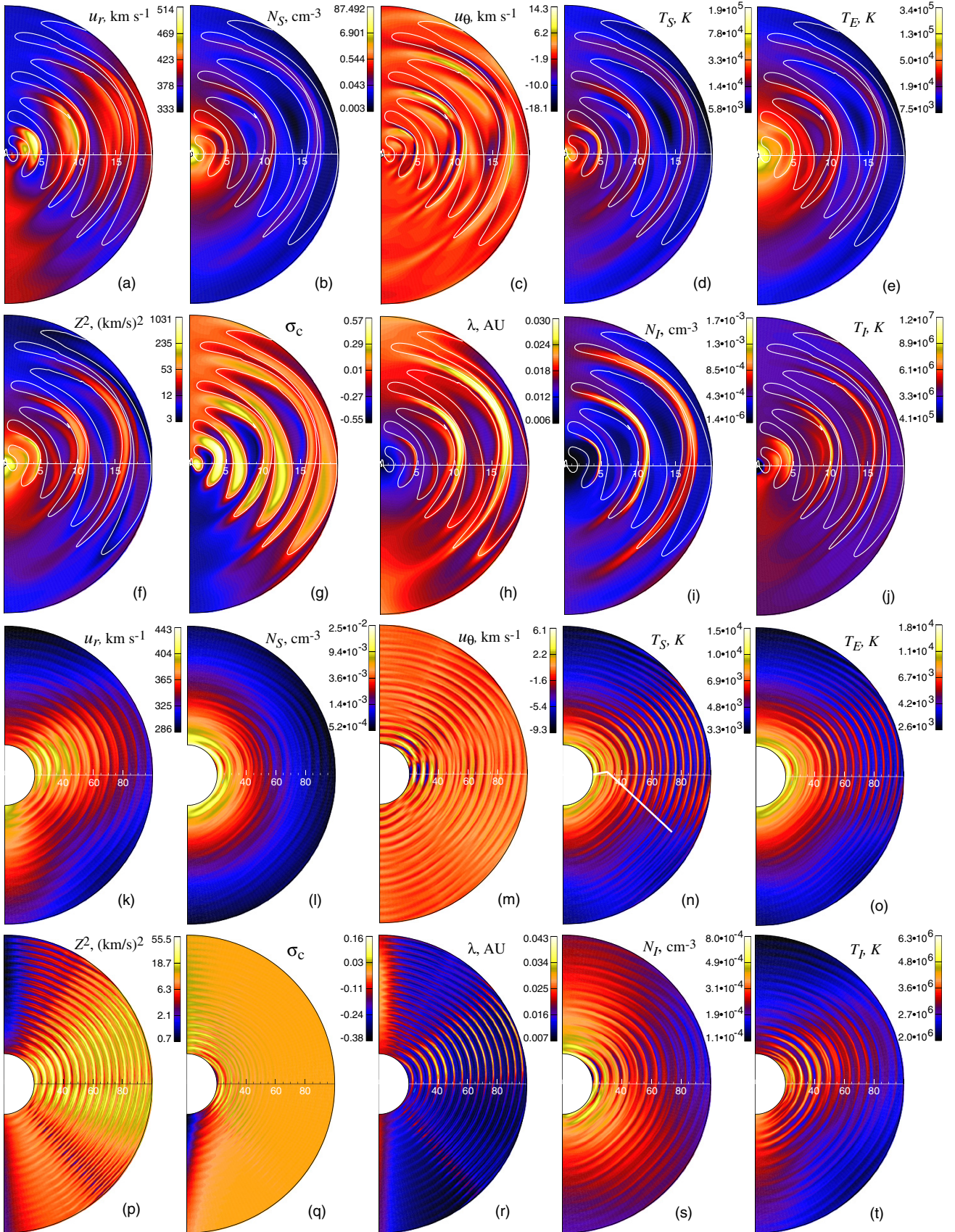


Figure 11. Contour plots in the meridional plane $\phi = 0^\circ 75$ from 0.3 to 20 AU (a–j) and from 20 to 100 AU (k–t) of the mean-flow and turbulence parameters for Carrington Rotation 2123. The white lines in (a–j) depict the heliospheric neutral sheet ($B_r = 0$). The white line in the plot (n) shows the projection of the *Voyager 2* trajectory on the meridional plane.

(A color version of this figure is available in the online journal.)

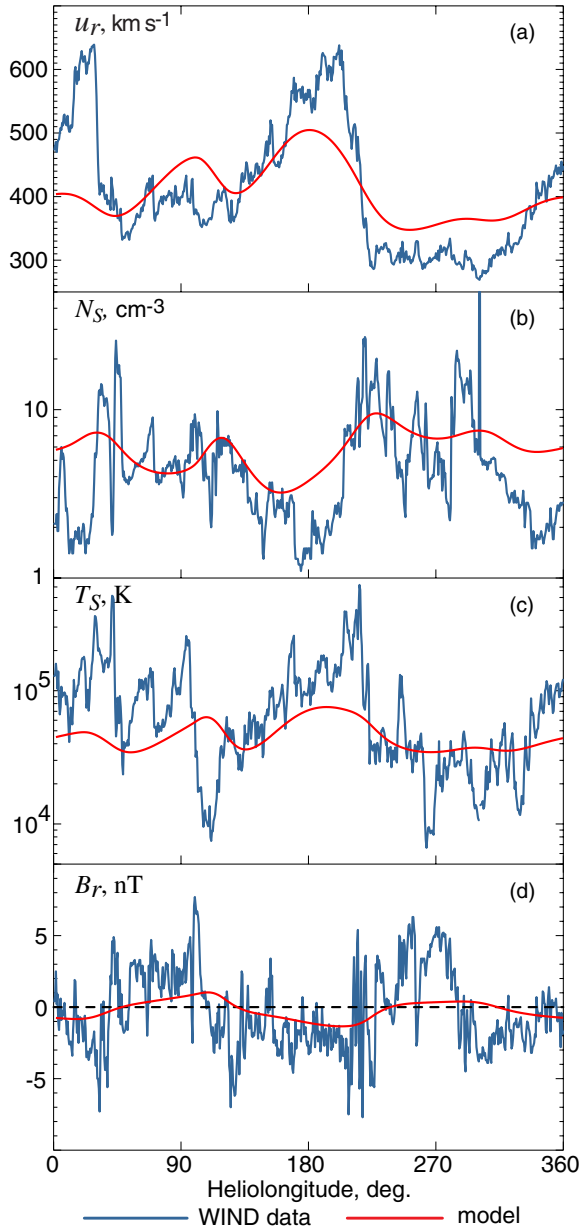


Figure 12. Results of simulation for Carrington Rotation 2123 at 1 AU in comparison with observations. The hourly averaged solar wind parameters observed by the *WIND* spacecraft are shown by blue lines: the radial velocity u_r (a), the number density of solar wind protons N_S (b), the proton temperature T_S (c), and the radial magnetic field B_r (d). The red lines are the calculated parameters.

(A color version of this figure is available in the online journal.)

Simulation with time-varying boundary conditions at the coronal base would be highly desirable.

2. A corollary of the assumption that the solutions are steady in the rotating frame is that the neutral hydrogen distribution is overly simplistic being a function only of radius and independent of longitude. We plan to include the direction of in-flow of the interstellar hydrogen from the interstellar medium into future time-dependent simulations.
3. The solar wind model with turbulence transport presented in this paper is only applicable to the super-Alfvénic solar wind flow because the turbulence transport model at present employs the assumption that the flow velocity is much larger

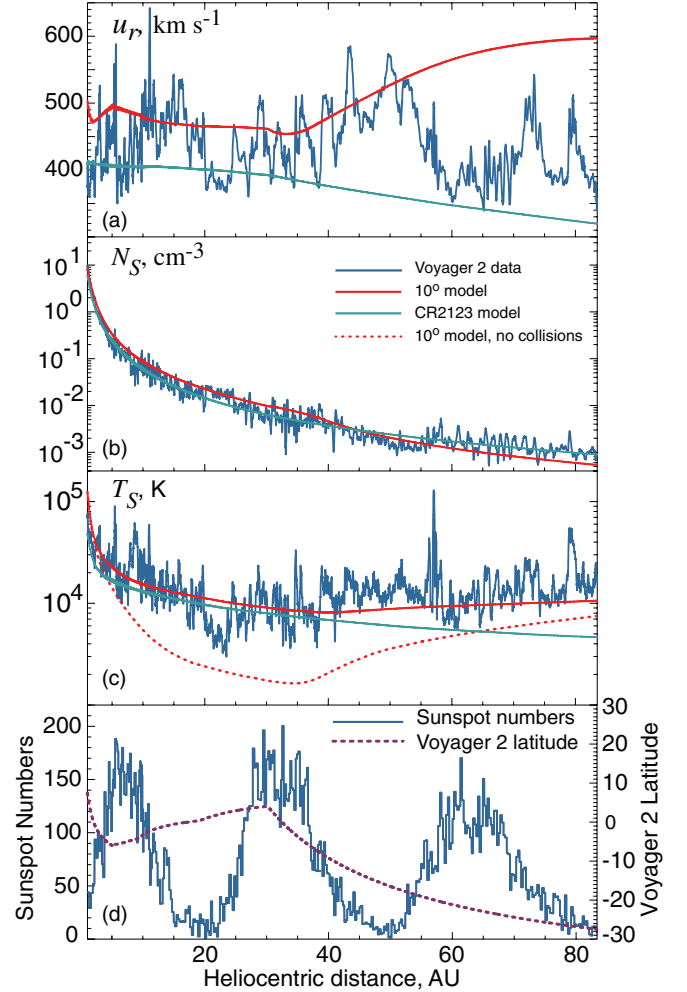


Figure 13. Radial variations of radial velocity u_r (a), solar proton density N_S (b), and solar proton temperature T_S (c) computed along the trajectory of *Voyager 2* for the magnetic field on the Sun represented either by a magnetic dipole tilted by 10° (red lines) or the observed magnetic field during Carrington Rotation 2123 (light blue lines); The dotted line in (c) is T_S computed with the 10° tilted-dipole model with no Coulomb collisions. The dark blue lines in plots (a–c) depict plasma parameters observed by *Voyager 2*. Both the observed and model parameters are represented by 27 day running averages. The bottom plot shows the monthly sunspot numbers and heliographic latitude of *Voyager 2*. Note that the 10° tilted-dipole model is representative of periods near solar minimum, while the Carrington Rotation 2123 is close to the last solar activity maximum. (A color version of this figure is available in the online journal.)

than the Alfvén velocity. We plan to relax this limitation of the turbulence transport model and to replace the WKB-Alfvén-wave approach within 0.3 AU with a generalized turbulence transport model.

4. Following Breech et al. (2008) and Breech et al. (2009), the normalized energy difference σ_D , the isotropization parameter f_D , the fraction of turbulent energy absorbed by protons f_p , and the proton–electron collision time scale τ_{SE} are all treated as constant parameters in the present model. Acting like a closure, the $\sigma_D = \text{const}$ approximation greatly simplifies equations, but it is justified mainly by observations of the Alfvén ratio in the solar wind (Matthaeus & Goldstein 1982; Tu & Marsch 1995). The Alfvén ratio (r_A , the ratio of kinetic to magnetic energy of fluctuations) is often observed to be close to 0.5, which corresponds to the value of $\sigma_D = (r_A - 1)/(r_A + 1) = -1/3$ used in the present

study. Nevertheless, incorporating an evolution equation for σ_D (see, e.g., Zhou & Matthaeus 1990; Tu & Marsch 1993; Yokoi et al. 2008; Zank et al. 2012) is among obvious future model improvements. Isenberg (2005) suggested that in general f_D should be a function of the radial velocity u_r , Alfvén velocity V_A , and the turbulence energy Z^2 . Cranmer et al. (2009) demonstrated that the turbulence energy partition between solar wind electrons and protons, f_p , can depend on the radial distance. It is obvious that the collision time scale τ_{SE} should also be radially dependent. We plan to study the possible variations of the model parameters in future work.

5. While the mean-flow solar wind is fully compressible, the turbulence is assumed to be incompressible and we neglect all fluctuations of the densities and thermal pressures, $N'_S = N'_I = 0$ and also $P'_S = P'_I = P'_E = 0$. Although, the fluctuations observed in the solar wind are mainly of the incompressible type (Belcher & Davis 1971; Matthaeus et al. 1990), it would be a natural development to allow the fluctuations to be compressible.
6. By replacing the anisotropic Reynolds stress tensor approximation (20) with the eddy viscosity approximation (22), we have added the important effect of shear driving, but left out the transverse approximation (built into Equation (20)) assuming that fluctuations are isotropic. Since the fluctuations observed in the solar wind are typically transverse to the mean magnetic field (e.g., Belcher & Davis 1971), it is desirable to incorporate the transverse condition into the eddy viscosity approximation. One possibility is to replace the isotropic term in Equation (22) with (20).
7. A significant limitation of the Reynolds averaging approach, in which fluctuations of all scales are integrated, is that the model constants C_β and C_γ (see Equation (26) and Section 2.4) are free parameters that can be only derived from relatively simple simulations that allow comparing results from direct numerical simulation with those from turbulence modeling. Meanwhile, it is known that the empirical estimates can be affected by the specific external conditions of the simulation. The most promising approach to overcome this difficulty is to employ the large eddy simulation (LES) or filtering approach, in which spatial coarse-graining is applied and only small-scale unresolved motions are modeled. The basic idea of LES is that resolving large-scale eddies reduces the scope of turbulence modeling and therefore the error that the modeling introduces. In addition, small-scale motions are typically more isotropic and less dependent on the external conditions. In the so-called dynamic version of LES (Germano et al. 1991; Germano 1992; Meneveau & Katz 2000) values of model constants are obtained in the course of simulation from the condition that global physical observables are independent of grid resolution.

We are currently investigating extensions of the current model in these directions, with the goal of a completely physics-based cross-scale dynamical model for the solar wind.

The authors are indebted to Sean Oughton for his results used in Appendix B. We also gratefully acknowledge Nobumitsu Yokoi and Robert Rubinstein for valuable discussions. The spacecraft data used in this study were obtained from the NASA/GSFC's Space Physics Data Facility's OMNIWeb service at <http://omniweb.gsfc.nasa.gov>. John M. Wilcox Solar Observatory data used in this study were obtained via the web site

<http://wso.stanford.edu> courtesy of J. T. Hoeksema. The work of A.V.U. was supported by NSF grant AST-1004035 and NASA grants NNX09AH79G and NNX13AR42G to the University of Delaware. Supercomputer time allocations were provided by the NASA High-End Computing (HEC) Program awards SMD-12-3050 and SMD-13-4027 through the NASA Advanced Supercomputing (NAS) Division at the Ames Research Center and the NASA Center for Climate Simulation (NCCS) at the Goddard Space Flight Center.

APPENDIX A

THE TURBULENCE TRANSPORT EQUATIONS

Subtracting Equation (9) from Equation (2) and Equation (10) from Equation (3), we obtain the equations for the fluctuating quantities \mathbf{v}' and \mathbf{b}' in the form

$$\begin{aligned} \frac{\partial \mathbf{v}'}{\partial t} = & -(\mathbf{v} \cdot \nabla) \mathbf{v}' - (\mathbf{v}' \cdot \nabla) \mathbf{v} - (\mathbf{v}' \cdot \nabla) \mathbf{v}' + (\mathbf{V}_A \cdot \nabla) \mathbf{b}' \\ & - \mathbf{b}'(\nabla \cdot \mathbf{V}_A) + (\mathbf{b}' \cdot \nabla) \mathbf{V}_A - \mathbf{V}_A(\nabla \cdot \mathbf{b}') \\ & + (\mathbf{b}' \cdot \nabla) \mathbf{b}' - \mathbf{b}'(\nabla \cdot \mathbf{b}') \\ & - \frac{1}{\rho} \nabla \bar{P}' + \frac{1}{\rho} \nabla \cdot \mathcal{R} - \frac{1}{\rho} (q_{ex1} + q_{ex2} + q_{ph}) m_p \mathbf{v}' - 2\mathbf{\Omega} \times \mathbf{v}', \quad (A1) \end{aligned}$$

$$\begin{aligned} \frac{\partial \mathbf{b}'}{\partial t} = & (\mathbf{b}' \cdot \nabla) \mathbf{v} + (\mathbf{V}_A \cdot \nabla) \mathbf{v}' - (\mathbf{v} \cdot \nabla) \mathbf{b}' \\ & - (\mathbf{v}' \cdot \nabla) \mathbf{V}_A - \frac{\mathbf{b}'}{2} \nabla \cdot \mathbf{v} - \frac{\mathbf{V}_A}{2} \nabla \cdot \mathbf{v}' \\ & + (\mathbf{b}' \cdot \nabla) \mathbf{v}' - (\mathbf{v}' \cdot \nabla) \mathbf{b}' - \frac{\mathbf{b}'}{2} \nabla \cdot \mathbf{v}' - \frac{\nabla \times (\rho^{1/2} \mathbf{\epsilon}_m)}{\rho^{1/2}} - \frac{\mathbf{b}'}{2\rho} q_{ph} m_p, \quad (A2) \end{aligned}$$

where $\bar{P}' = P'_S + P'_E + P'_I + [B'^2 + 2(\mathbf{B} \cdot \mathbf{B}') - \langle B'^2 \rangle]/8\pi$ is the fluctuation of the total of thermal and magnetic pressures. Multiplying Equation (A1) by \mathbf{v}' and Equation (A2) by \mathbf{b}' , adding the resulting equations, and applying the Reynolds averaging, we obtain the following equation for Z^2 ,

$$\begin{aligned} \frac{\partial Z^2}{\partial t} = & -(\mathbf{v} \cdot \nabla) Z^2 - \frac{Z^2}{2} \nabla \cdot \mathbf{u} - \frac{2}{\rho} \mathcal{R} : \nabla \mathbf{u} \\ & + \frac{\sigma_D Z^2}{2} \nabla \cdot \mathbf{u} - 2\mathbf{\epsilon}_m \cdot (\nabla \times \mathbf{V}_A) \\ & + (\mathbf{V}_A \cdot \nabla)(Z^2 \sigma_c) - Z^2 \sigma_c \nabla \cdot \mathbf{V}_A - \frac{2}{\rho} \langle (\mathbf{v}' \cdot \nabla) \bar{P}' \rangle \\ & - 2 \langle (\mathbf{v}' \cdot \mathbf{V}_A) \nabla \cdot \mathbf{b}' \rangle \\ & - \langle (\mathbf{b}' \cdot \mathbf{V}_A) \nabla \cdot \mathbf{v}' \rangle - \frac{m_p Z^2}{2\rho} [2(q_{ex1} \\ & + q_{ex2})(\sigma_D + 1) + q_{ph}(\sigma_D + 3)] + NL_1, \quad (A3) \end{aligned}$$

where NL_1 consolidates the nonlinear terms. Similarly, multiplying Equation (A1) by \mathbf{b}' and Equation (A2) by \mathbf{v}' , adding the resulting equations, and applying Reynolds averaging, we obtain the equation for $Z^2 \sigma_c$

$$\begin{aligned} \frac{\partial (Z^2 \sigma_c)}{\partial t} = & -(\mathbf{v} \cdot \nabla)(Z^2 \sigma_c) + (\mathbf{V}_A \cdot \nabla) Z^2 \\ & - \frac{Z^2 \sigma_c}{2} \nabla \cdot \mathbf{u} - \frac{2}{\rho} \mathcal{R} : \nabla \mathbf{V}_A - 2\mathbf{\epsilon}_m \cdot (\nabla \times \mathbf{u}) \end{aligned}$$

$$\begin{aligned}
& - \frac{1}{2\rho} [2(q_{\text{ex1}} + q_{\text{ex2}}) + 3q_{\text{ph}}] m_p Z^2 \sigma_c - (1 - \sigma_D) Z^2 \nabla \cdot \mathbf{V}_A \\
& - 2\langle (\mathbf{b}' \cdot \mathbf{V}_A) \nabla \cdot \mathbf{b}' \rangle \\
& - \frac{2}{\rho} \langle (\mathbf{b}' \cdot \nabla) \bar{P}' \rangle - \langle (\mathbf{v}' \cdot \mathbf{V}_A) \nabla \cdot \mathbf{v}' \rangle + NL_2, \quad (\text{A4})
\end{aligned}$$

where NL_2 again consolidates the nonlinear terms. Neglecting the terms $-(2/\rho)\langle (\mathbf{v}' \cdot \nabla) \bar{P}' \rangle$ and $-(2/\rho)\langle (\mathbf{b}' \cdot \nabla) \bar{P}' \rangle$ (see the discussion in Zhou & Matthaeus 1990) and also all the terms containing \mathbf{V}_A , which are presumably small in the highly super-Alfvénic solar wind beyond 0.3 AU, we arrive at the following equations

$$\begin{aligned}
\frac{\partial Z^2}{\partial t} &= -(\mathbf{v} \cdot \nabla) Z^2 - \frac{Z^2}{2} \nabla \cdot \mathbf{u} - \frac{2}{\rho} \mathcal{R} : \nabla \mathbf{u} + \frac{\sigma_D Z^2}{2} \nabla \cdot \mathbf{u} \\
& - \frac{m_p Z^2}{2\rho} [2(q_{\text{ex1}} + q_{\text{ex2}})(\sigma_D + 1) + q_{\text{ph}}(\sigma_D + 3)] + NL_1, \quad (\text{A5})
\end{aligned}$$

and

$$\begin{aligned}
\frac{\partial (Z^2 \sigma_c)}{\partial t} &= -(\mathbf{v} \cdot \nabla)(Z^2 \sigma_c) - \frac{Z^2 \sigma_c}{2} \nabla \cdot \mathbf{u} - 2\boldsymbol{\varepsilon}_m \cdot (\nabla \times \mathbf{u}) \\
& - \frac{1}{2\rho} [2(q_{\text{ex1}} + q_{\text{ex2}}) + 3q_{\text{ph}}] m_p Z^2 \sigma_c + NL_2. \quad (\text{A6})
\end{aligned}$$

If Equation (20) is employed as an approximation for \mathcal{R} then

$$-\frac{2}{\rho} \mathcal{R} : \nabla \mathbf{u} = \sigma_D Z^2 [\hat{\mathbf{B}} \cdot (\hat{\mathbf{B}} \cdot \nabla) \mathbf{u} - \nabla \cdot \mathbf{u}],$$

and Equations (A5) and (A6) are reduced to those used by Usmanov et al. (2009, 2011, 2012). Note that (1) the structural similarity assumption was not used in deriving Equations (A5) and (A6); (2) the nonlinear terms, NL_1 and NL_2 , are modeled separately (see Breech et al. 2008); and (3) we assume that Equation (18) for the evolution of the correlation length λ retains the form used by Breech et al. (2008) and Usmanov et al. (2009, 2011, 2012).

APPENDIX B

THE MEAN TURBULENT ENERGY DISSIPATION RATE

Using direct numerical simulations of stationary and isotropic hydrodynamic turbulence, Pearson et al. (2004) studied the dependence on the Reynolds number of the non-dimensional kinetic energy dissipation rate,

$$C_\varepsilon = \varepsilon L / u'^2, \quad (\text{B1})$$

where ε is the mean turbulent energy dissipation rate per unit mass, and L and u' are characteristic length and velocity scales, respectively, of the energy containing eddies. Pearson et al. (2004) arrived at the conclusion that the asymptotic value for C_ε at high Reynolds number is ≈ 0.5 . Assuming that this result can be employed in the MHD case, we use it to estimate the Kármán–Taylor constant, α , in the turbulence transport Equations (16)–(18).

Pearson et al. (2004) define L as

$$L = \frac{\pi}{2u'^2} \int_0^\infty k^{-1} E(k) dk, \quad (\text{B2})$$

where $E(k)$ is the energy density spectrum function, k is the scalar wavenumber magnitude, and the characteristic velocity scale u' is related to the amplitude of velocity fluctuations, $\langle v'^2 \rangle^{1/2}$, as $u'^2 = \langle v'^2 \rangle / 3$. The definition of the correlation length λ (see, e.g., Breech et al. 2008) in the case of isotropic hydrodynamic turbulence reduces to

$$\lambda = \frac{1}{\langle v'^2 \rangle} \int_0^\infty R_{ii}(\zeta) d\zeta, \quad (\text{B3})$$

where R_{ii} is the trace of the two-point correlation function $R_{ij} = \langle v'_i(\mathbf{r}) v'_j(\mathbf{r} + \boldsymbol{\zeta}) \rangle$ and $\boldsymbol{\zeta}$ is the spatial lag. It is straightforward to show (Batchelor 1959) that

$$\int_0^\infty R_{ii}(\zeta) d\zeta = \pi \int_0^\infty k^{-1} E(k) dk, \quad (\text{B4})$$

and then from Equations (B2)–(B4) it follows that $L = 3\lambda/2$. Correspondingly, the equation for the decay of turbulent kinetic energy takes the form

$$\frac{\partial}{\partial t} \frac{\langle v'^2 \rangle}{2} = -\varepsilon = -\frac{2C_\varepsilon}{9\sqrt{3}} \frac{\langle v'^2 \rangle^{3/2}}{\lambda}. \quad (\text{B5})$$

In the MHD case, if there is neither transport nor production of turbulence and in the absence of cross helicity effects ($\sigma_c = 0$ and then $f^+(\sigma_c) = 1$), Equation (16) reduces to

$$\frac{\partial Z^2}{\partial t} = \alpha \frac{Z^3}{\lambda}. \quad (\text{B6})$$

From comparison of Equations (B5) and (B6) we obtain the following relation between α and C_ε ,

$$\alpha = \frac{4C_\varepsilon}{9\sqrt{3}}. \quad (\text{B7})$$

The expression for ε in the MHD case then takes the form

$$\varepsilon = \frac{2C_\varepsilon}{9\sqrt{3}} \frac{Z^3}{\lambda}. \quad (\text{B8})$$

REFERENCES

- Batchelor, G. K. 1959, *The Theory of Homogeneous Turbulence* (Cambridge: Cambridge Univ. Press)
- Belcher, J. W., & Davis, L. 1971, *JGR*, **76**, 3534
- Biskamp, D. 2008, *Magnetohydrodynamic Turbulence* (Cambridge: Cambridge Univ. Press)
- Borovsky, J. E. 2006, *PhPl*, **13**, 056505
- Boussinesq, J. 1877, *Mémoires présentés par divers savants à l'Académie des Sciences*, 23
- Breech, B., Matthaeus, W. H., Cranmer, S. R., Kasper, J. C., & Oughton, S. 2009, *JGR*, **114**, A09103
- Breech, B., Matthaeus, W. H., Minnie, J., et al. 2008, *JGR*, **113**, A08105
- Burlaga, L. F., Ness, N. F., Belcher, J. W., & Whang, Y. C. 1996, *JGR*, **101**, 15523
- Burlaga, L. F., Ness, N. F., Belcher, J. W., et al. 1994, *JGR*, **99**, 21511
- Chalov, S. V., Alexashov, D. B., & Fahr, H. J. 2006, *AstL*, **32**, 206
- Chen, Y., & Hu, Y. Q. 2001, *SoPh*, **199**, 371
- Cranmer, S. R., Matthaeus, W. H., Breech, B. A., & Kasper, J. C. 2009, *ApJ*, **702**, 1604
- Cuperman, S., Detman, T. R., & Dryer, M. 1988, *ApJ*, **330**, 466
- Davila, J. M., & Ofman, L. 1999, *SSRv*, **87**, 165

- Detman, T. R., Intriligator, D. S., Dryer, M., et al. 2011, *JGR*, **116**, A03105
- Durney, B. R. 1973, *SoPh*, **30**, 223
- Endeve, E., Holzer, T. E., & Leer, E. 2004, *ApJ*, **603**, 307
- Esser, R., Leer, E., Habbal, S. R., & Withbroe, G. L. 1986, *JGR*, **91**, 2950
- Fite, W. L., Smith, A. C. H., & Stebbings, R. F. 1962, *RSPSA*, **268**, 527
- Gamayunov, K. V., Zhang, M., Pogorelov, N. V., Heerikhuisen, J., & Rassoul, H. K. 2012, *ApJ*, **757**, 74
- Germano, M. 1992, *JFM*, **238**, 325
- Germano, M., Piomelli, U., Moin, P., & Cabot, W. H. 1991, *PhFl*, **3**, 1760
- Gottlieb, S., Shu, C.-W., & Tadmor, E. 2001, *SIAMR*, **43**, 89
- Habbal, S. R., Esser, R., Guhathakurta, M., & Fisher, R. R. 1995, *GeoRL*, **22**, 1465
- Hartle, R. E., & Barnes, A. 1970, *JGR*, **75**, 6915
- Hartle, R. E., & Sturrock, P. A. 1968, *ApJ*, **151**, 1155
- Hollweg, J. V. 1973, *ApJ*, **181**, 547
- Hollweg, J. V. 1974, *JGR*, **79**, 3845
- Hollweg, J. V. 1976, *JGR*, **81**, 1649
- Holzer, T. E. 1972, *JGR*, **77**, 5407
- Hu, Y. Q., Habbal, S. R., Chen, Y., & Li, X. 2003a, *JGR*, **108**, 1377
- Hu, Y. Q., Li, X., & Habbal, S. R. 2003b, *JGR*, **108**, 1378
- Isenberg, P. A. 1986, *JGR*, **91**, 9965
- Isenberg, P. A. 2005, *ApJ*, **623**, 502
- Isenberg, P. A., & Feldman, W. C. 1995, *GeoRL*, **22**, 873
- Isenberg, P. A., Smith, C. W., & Matthaeus, W. H. 2003, *ApJ*, **592**, 564
- Isenberg, P. A., Smith, C. W., Matthaeus, W. H., & Richardson, J. D. 2010, *ApJ*, **719**, 716
- Jacques, S. A. 1978, *ApJ*, **226**, 632
- Kraichnan, R. H. 1964, *PhFl*, **7**, 1048
- Kryukov, I. A., Pogorelov, N. V., Zank, G. P., & Borovikov, S. N. 2012, in AIP Conf. Proc. 1436, Physics of the Heliosphere: A 10 Year Retrospective, ed. J. Heerikhuisen, G. Li, N. V. Pogorelov, & G. P. Zank (Melville, NY: AIP), 48
- Kurganov, A., & Levy, D. 2000, *SIAM J. Sci. Comput.*, **22**, 1461
- Leer, E., & Axford, W. I. 1972, *SoPh*, **23**, 238
- Leslie, D. C. 1973, *Developments in the Theory of Turbulence* (Oxford: Clarendon)
- Li, B., Li, X., Hu, Y. Q., & Habbal, S. R. 2004, *JGR*, **109**, A07103
- Marsch, E., & Tu, C. Y. 1992, in Solar Wind Seven, ed. E. Marsch & R. Schwenn (Oxford: Pergamon), 505
- Matthaeus, W. H., & Goldstein, M. L. 1982, *JGR*, **87**, 6011
- Matthaeus, W. H., Goldstein, M. L., & Roberts, D. A. 1990, *JGR*, **95**, 20673
- Matthaeus, W. H., Minnie, J., Breech, B., et al. 2004, *GeoRL*, **31**, L12803
- Matthaeus, W. H., Zank, G. P., Smith, C. W., & Oughton, S. 1999, *PhRvL*, **82**, 3444
- Meneveau, C., & Katz, J. 2000, *AnRFM*, **32**, 1
- Meyer-Vernet, N. 2007, *Basics of the Solar Wind* (Cambridge: Cambridge Univ. Press)
- Pearson, B. R., Yousef, T. A., Haugen, N. E. L., Brandenburg, A., & Krogstad, P.-Å. 2004, *PhRvE*, **70**, 056301
- Pei, C., Bieber, J. W., Breech, B., et al. 2010, *JGR*, **115**, A03103
- Pilipp, W. G., Miggenrieder, H., Mühlhäuser, K.-H., Rosenbauer, H., & Schwenn, R. 1990, *JGR*, **95**, 6305
- Pizzo, V. J. 1978, *JGR*, **83**, 5563
- Pizzo, V. J. 1982, *JGR*, **87**, 4374
- Pogorelov, N. V., Borovikov, S. N., Zank, G. P., & Ogino, T. 2009, *ApJ*, **696**, 1478
- Powell, K. G. 1994, An Approximate Riemann Solver for Magnetohydrodynamics, (that Works in More Than One Dimension), Technical Report ICASE No. 94-24 (Hampton, VA: Institute for Computer Applications in Science and Engineering)
- Rucinski, D., & Fahr, H. J. 1989, *A&A*, **224**, 290
- Ruderman, M. S., Goldstein, M. L., Roberts, D. A., Deane, A. E., & Ofman, L. 1999, *JGR*, **104**, 17,057
- Sandbæk, Ø., & Leer, E. 1994, *ApJ*, **423**, 500
- Sandbæk, Ø., Leer, E., & Holzer, T. E. 1992, *ApJ*, **400**, 362
- Scime, E. E., Badeau, A. E., & Littleton, J. E. 1999, *GeoRL*, **26**, 2129
- Semar, C. L. 1970, *JGR*, **75**, 6892
- Smith, C. W., Isenberg, P. A., Matthaeus, W. H., & Richardson, J. D. 2006, *ApJ*, **638**, 508
- Smith, C. W., Matthaeus, W. H., Zank, G. P., et al. 2001, *JGR*, **106**, 8253
- Sokolov, I. V., van der Holst, B., Oran, R., et al. 2013, *ApJ*, **764**, 23
- Sturrock, P. A., & Hartle, R. E. 1966, *PhRvL*, **16**, 628
- Suess, S. T., Wang, A.-H., Wu, S. T., Poletto, G., & McComas, D. J. 1999, *JGR*, **104**, 4697
- Tu, C.-Y., & Marsch, E. 1993, *JGR*, **98**, 1257
- Tu, C.-Y., & Marsch, E. 1995, *SSRv*, **73**, 1
- Tu, C.-Y., & Marsch, E. 1997, *SoPh*, **171**, 363
- Usmanov, A. V. 1993, *SoPh*, **146**, 377
- Usmanov, A. V. 1996, in Solar Wind 8 Conference, ed. D. Winterhalter, J. T. Gosling, S. R. Habbal, W. S. Kurth, & M. Neugebauer (Woodbury, NY: AIP), 141
- Usmanov, A. V., & Goldstein, M. L. 2003, *JGR*, **108**, 1354
- Usmanov, A. V., & Goldstein, M. L. 2006, *JGR*, **111**, A07101
- Usmanov, A. V., Goldstein, M. L., Besser, B. P., & Fritzer, J. M. 2000, *JGR*, **105**, 12675
- Usmanov, A. V., Goldstein, M. L., & Matthaeus, W. H. 2012, *ApJ*, **754**, 40
- Usmanov, A. V., Matthaeus, W. H., Breech, B., & Goldstein, M. L. 2009, in ASP Conf. Ser. 406, Numerical Modeling of Space Plasma Flows: ASTRONUM-2008, ed. N. V. Pogorelov, E. Audit, P. Colella, & G. P. Zank (San Francisco, CA: ASP), 160
- Usmanov, A. V., Matthaeus, W. H., Breech, B., & Goldstein, M. L. 2011, *ApJ*, **727**, 84
- van der Holst, B., Manchester, W. B., Frazin, R. A., et al. 2010, *ApJ*, **725**, 1373
- Wang, C., & Richardson, J. D. 2001, *JGR*, **106**, 29401
- Wang, C., Richardson, J. D., & Gosling, J. T. 2000, *JGR*, **105**, 2337
- Whang, Y. C. 1998, *JGR*, **103**, 17419
- Whang, Y. C. 2010, *ApJ*, **713**, 721
- Whang, Y. C., Burlaga, L. F., & Ness, N. F. 1995, *JGR*, **100**, 17015
- Whang, Y. C., Burlaga, L. F., Wang, Y.-M., & Sheeley, N. R. 2003, *ApJ*, **589**, 635
- Williams, L. L., Zank, G. P., & Matthaeus, W. H. 1995, *JGR*, **100**, 17059
- Yokoi, N. 2013, *GApFD*, **107**, 114
- Yokoi, N., Higashimori, K., & Hoshino, M. 2013, *PhPl*, **20**, 122310
- Yokoi, N., Rubinstein, R., Yoshizawa, A., & Hamba, F. 2008, *JTurbo*, **9**, 1
- Yoshizawa, A. 1984, *PhFl*, **27**, 1377
- Yoshizawa, A. 1998, *Hydromagnetic and Magnetohydrodynamic Turbulent Flows: Modeling and Statistical Theory* (Dordrecht: Kluwer)
- Zank, G. P. 1999, *SSRv*, **89**, 413
- Zank, G. P., Dosch, A., Hunana, P., et al. 2012, *ApJ*, **745**, 35
- Zank, G. P., & Pauls, H. L. 1997, *JGR*, **102**, 7037
- Zhao, X., & Hoeksema, J. T. 1995, *JGR*, **100**, 19
- Zhou, Y., & Matthaeus, W. H. 1990, *JGR*, **95**, 10291